Separation of the optical and mass features of particle components in different aerosol mixtures by using POLIPHON retrievals in synergy with continuous polarized Micro-Pulse Lidar (P-MPL) measurements

Carmen Córdoba-Jabonero[1][*], Michaël Sicard[2,3], Albert Ansmann[4], Ana del Águila[1], and Holger Baars[4]

[1]Instituto Nacional de Técnica Aeroespacial (INTA), Atmospheric Research and Instrumentation Branch, Torrejón de Ardoz (Madrid), Spain
[2]CommSensLab, Dept. of Signal Theory and Communications, Universitat Politècnica de Catalunya (UPC), Barcelona, Spain
[3]Ciències i Tecnologies de l'Espai - Centre de Recerca de l'Aeronàutica i de l'Espai/Institut d'Estudis Espacials de Catalunya (CTE-CRAE/IEEC), Universitat Politècnica de Catalunya, Barcelona, Spain
[4]Leibniz Institute for Tropospheric Research (TROPOS), Leipzig, Germany

Correspondence to: Carmen Córdoba-Jabonero (cordobajc@inta.es)

Abstract. The application of the POLIPHON (POlarization-LIdar PHOtometer Networking) method in synergy with continuous 24/7 polarized Micro-Pulse Lidar (P-MPL) measurements to derive the vertical separation of two/three particle components in different aerosol mixtures, and the retrieval of their particular optical properties, is presented for the first time. The procedure of extinction-to-mass conversion, together with an analysis of the Mass Extinction Efficiency (MEE) parameter, is described, and the relative mass contribution of each aerosol component is also derived in a further step. The general POLIPHON algorithm is based on the specific particle linear depolarization ratio given for different types of aerosols, and can be run in either 1-step (POL-1) or 2 steps (POL-2) versions in dependence on the either 2- or 3-component separation. In order to illustrate this procedure aerosol mixing cases observed over Barcelona (NE Spain) are selected: a dust event occurred on 5 July 2016; smoke plumes detected on 23 May 2016; and a pollination episode observed on 23 March 2016. In particular, the 3-component separation is just applied for the dust case: a combined POL-1 with POL-2 procedure (POL-1/2) is used, and additionally the dust fine contribution to the total fine mode (dust fine plus non-dusty aerosols) is estimated. The high dust impact occurs before 12:00 UTC yields a mean mass loading of 0.6 ± 0.1 g m^{-2} due to the prevalence of Saharan dust coarse particles. After that time, the mean mass loading is reduced by two thirds, showing a rather weak dust incidence. In the smoke case, the arrival of fine biomass burning particles is detected at altitudes as high as 7 km height. The smoke particles, probably mixed with less depolarizing non-smoke aerosols, are observed in air masses having their origin from either North America fires or the Arctic area, as reported by HYSPLIT backtrajectory analysis. The particle linear depolarization ratio for smoke shows values in the 0.10-0.15 range, even higher at given times, and the daily mean smoke mass loading is 0.017 ± 0.008 g m^{-2}, around 3 % out of that found for the dusty event. Pollen particles are detected up to 1.5 km height from 10:00 UTC on during an intense pollination event with a particle linear depolarization ratio ranging between 0.10 and 0.15. The maximal mass loading of *Platanus* pollen particles is 0.011 ± 0.003 g m^{-2}, representing around 2 % out of the dust loading during the higher dust incidence. Regarding the MEE derived for each aerosol component,

their values are in agreement with others referenced in the literature for the specific aerosol types examined in this work: 0.5 ± 0.1 m^2 g^{-1} and 1.7 ± 0.2 m^2 g^{-1} are found for dust coarse and fine particles, respectively; 4.5 ± 1.4 m^2 g^{-1} is derived for smoke, and 2.4 ± 0.5 m^2 g^{-1} for non-smoke aerosols with Arctic origin (a MEE value close to that reported for Arctic aerosols: 2.17 m^2 g^{-1}, as supposed larger aerosols than those biomass burning particles); and a MEE of 2.4 ± 0.8 m^2 g^{-1} is obtained for pollen particles, though it can reach higher/lower values depending on a predominant smaller/larger size of the pollen grains. Results reveal the high potential of the P-MPL system, a simple polarization-sensitive elastic backscatter lidar working in a 24/7 operation mode, to retrieve the relative optical and mass contributions of each aerosol component along all the day, reflecting the daily variability of their properties. In fact, this procedure can be simply implemented in other P-MPLs also operating within the world-wide Micro-Pulse Lidar Network (MPLNET), thus extending the aerosol discrimination at a global scale. Moreover, the method has the advantage to be relatively easily applicable also to spaceborne lidars with an equivalent configuration such as the ongoing Cloud-Aerosol Lidar with Orthogonal Polarization (CALIOP) onboard NASA/CALIPSO (Cloud-Aerosol Lidar and Infrared Pathfinder Satellite Observations), and the forthcoming Atmospheric Lidar (ATLID) onboard ESA/EarthCARE mission.

1 Introduction

It is widely known that atmospheric aerosols contribute to climate change due to their effects (direct and indirect) in the Earth's energy budget. Different types of aerosols present different radiative properties and thus contribute in a different way to climate change (Boucher et al., 2013; Myhre et al., 2013). As far as estimates of aerosol direct radiative forcing are concerned, the knowledge of the aerosol types under study is thus critical. The aerosol direct radiative properties involved in radiative transfer calculations are the particle extinction (scattering + absorption) coefficient, single scattering albedo (the ratio of scattering to extinction), asymmetry factor as defined as the intensity-weighted average cosine of the scattering angle, and their vertical distribution. Referring to the factors important in constraining the radiative effect of aerosols, Boucher et al. (2013) stated "Particularly important are the single scattering albedo (especially over land or above clouds) and the AOD", the aerosol optical depth, i.e. the column-integrated aerosol extinction. These two parameters can be estimated by or recalculated from the output of lidar-stand-alone algorithms such as Müller et al. (1999), Veselovskii et al. (2002) or Böckmann et al. (2005) which employ state-of-the-art elastic-Raman lidar measurements at several wavelengths. Such advanced measurements are scarce, however, compared with the large database of elastic lidar measurements worldwide.

For this reason, synergetic algorithms recently combine data from multi-wavelength elastic lidar and passive instrumentation to retrieve the extinction or both the extinction and the single scattering albedo at several wavelengths and discriminating between fine and coarse mode. Such algorithms are the LIdar-Radiometer Inversion Code-LIRIC (Chaikovsky et al., 2016), and the Generalized Aerosol Retrieval from Radiometer and LIDAR Combined data-GARRLiC (Lopatin et al., 2013). GARRLiC is embedded in a more generalized algorithm called the Generalized Retrieval of Atmosphere and Surface Properties inversion code-GRASP (Dubovik et al., 2014). The drawback of these algorithms is that they apply to at least three-wavelength elastic systems, while a majority of single- and dual-

wavelength elastic systems are operating worldwide. For such less sophisticated systems, the primary way of discriminating between aerosol types is to have a polarization-sensitive channel, where the discrimination is based on the comparison of the particle depolarization ratio measured with two reference particle depolarization ratio values.

75   Aerosol discrimination using particle depolarization was first formulated by Chen et al. (2001) and then used by Shimizu et al. (2004) for the observation of Asian dust in China and Japan with one elastic and one depolarization sensitive channel. Since 2009, the method has been used in an increasing number of studies to discriminate between dust and smoke (Tesche et al., 2009; 2011); ash and fine mode particles (Ansmann et al., 2011; 2012; Sicard et al., 2012); pollen and background particles (Noh et al., 2013; Sicard et al., 2016a). Very recently this method, known as

80   the POlarization-LIdar PHOtometer Networking (POLIPHON), has been refined by Mamouri and Ansmann (2014) to retrieve up to three aerosol components, such as fine and coarse dust and non-dust particles. POLIPHON is also the basis of the retrieval of ice nuclei number concentration in desert dust layers (Mamouri and Ansmann, 2015) and cloud condensation nucleus number concentration (Mamouri and Ansmann, 2016). In addition, a similar method is also used for separating aerosol mixtures in HSRL systems (Burton et al., 2012, 2014)

85   In addition to their effects on climate, atmospheric aerosols are also known to have an important impact on human health when they are inhaled. For example, exposure to anthropogenic particles (pollution) is clearly identified as a public health hazard causing acute and chronic effects to the respiratory and cardiovascular systems (Dockery et al., 1993; Künzli et al., 2000; WHO, 2003). Airborne pollen grains produced by wind-pollinated plants are responsible of allergenic reactions when inhaled by humans (Cecchi, 2013). More recently, Martiny and Chiapello (2013) highlighted

90   the role of desert dust on meningitis epidemics. Toxicological studies are currently aiming to identify which particle characteristics are responsible for which adverse health effects (e.g., particle number, mass, size, surface, chemical composition). Among these properties, what aerosol lidars can probably estimate the best is mass concentration when the aerosol type has been previously identified, and thus the relation between aerosol backscatter and extinction can be accurately related to specific aerosol physical properties. However, mass concentration retrievals from lidar data

95   are not common and there is very few information available on the vertical distribution of aerosol number and mass concentrations, although a number of field experiments involving research and commercial aircraft have measured aerosol concentrations (Heintzenberg et al.; 2011).

Mass concentration profiles can be estimated by multiplying the lidar-derived extinction coefficient by the mass extinction efficiency, sometimes also called the specific extinction cross-section, when the latter is known or can be

100   assumed. This conversion is often used to convert lidar-derived optical properties into mass concentration to test and evaluate transport models (Pérez et al., 2006; Sicard et al., 2015). Lately, POLIPHON is also used to extract from the total extinction the fractions of the high/moderate/low depolarizing particles which can then be converted separately into mass concentration (Mamouri and Ansmann, 2014; 2017). The method has been used for the estimation of the profile of mass concentration of dust (Ansmann et al., 2011; 2012), volcanic ash (Ansmann et al., 2012; Sicard et al.,

105   2012) and pollen (Sicard et al., 2016b). It is worth mentioning that another field that would greatly benefit from the knowledge of the aerosol mass concentration profile is the air traffic, as large particles can damage aircraft engines. By way of example, we recall the impact of the ash-loaded eruption plume from the Icelandic Eyjafjallajökull volcano on European air traffic in 2010 (Pappalardo et al., 2013).

The aim of this paper is to show the potential of simple lidar systems, with one elastic and one depolarization sensitive channel, to discriminate between several aerosol types and retrieve for each aerosol component the profiles of their optical properties and mass concentrations. The instrument used is the polarized version of the Micro-Pulse Lidar (P-MPL), the standard system within NASA/MPLNET (Micro Pulse Lidar NETwork) network (mplnet.gsfc.nasa.gov), sited in the Universitat Politècnica de Catalunya (UPC) at Barcelona (BCN) in northeastern Spain. The P-MPL is an elastic and monochromatic low-energy system which also includes a depolarization-sensitive channel, operating in an automatic and continuous 24/7 mode. The algorithm used to optically discriminate components in aerosol mixtures is the POLIPHON method, both 1-step and 2-step versions, in order to assess the vertical separation of a maximum of three aerosol components. The synergetic use of P-MPL/POLIPHON is tested with aerosol mixtures containing specific climate-relevant aerosols, namely desert dust, fire smoke and pollen. This is the first time that POLIPHON, well established for sophisticated powerful European Aerosol Research Lidar NETwork (EARLINET, www.earlinet.org) lidars, is applied to worldwide (MPLNET) and continuous simple elastic P-MPL measurements. Moreover, the method has the advantage to be relatively easily applicable also to spaceborne lidars with an equivalent configuration such as the ongoing Cloud-Aerosol Lidar with Orthogonal Polarization (CALIOP) onboard NASA/CALIPSO (Cloud-Aerosol Lidar and Infrared Pathfinder Satellite Observations) which has two elastic and one depolarization-sensitive channel, and the forthcoming Atmospheric Lidar (ATLID) onboard EarthCARE (future ESA mission to be launched in 2019) which will have a high-spectral resolution receiver and a depolarisation channel.

The paper is organized as follows: **Section 1** presents the introductory framework; the methodology is introduced in **Section 2**, which breaks down in the description of the measurement station and of the selected aerosol cases (**Sect. 2.1**), as well as the lidar system used in this paper (**Sect. 2.2**), an extended overview of the POLIPHON method (**Sect. 2.3**) and a detailed extinction-to-mass conversion procedure (**Sect. 2.4**); **Section 3** shows the results and their discussion for each case (dust, smoke and pollen). Finally, a summary of the work and the main conclusions are presented in **Section 4**. In addition, a list of acronyms (symbols) identifying the parameters/variables used in the work is shown in **Appendix A**.

2 Methodology

2.1 Measurement station and selected aerosol case studies

Barcelona (BCN) station is an urban site located at the North East Iberian Peninsula (41.4ºN, 2.1ºE, 115 m a.s.l.), along the coast of the Mediterranean Sea, on the North campus of UPC at the centre of Barcelona. The typical background aerosol is a mixing of polluted particles with a minor contribution of marine aerosols, only predominant under particular clean conditions; other aerosol types, such as desert dust, fire smoke, pollen, etc., are also frequently found (Sicard et al., 2011). BCN is a well-established EARLINET station, and a relatively new MPLNET site, where a polarized Micro-Pulse Lidar (P-MPL) is in routine operation since 2014. BCN is also a NASA/AERONET (Aerosol Robotic NETwork, aeronet.gsfc.nasa.gov) site, measuring AOD and the column-integrated aerosol optical properties during daytime (Holben et al., 1999).

In this work, three case studies of different aerosol mixtures (dust, fire smoke and pollen, all mixed with local background aerosols) observed over BCN are examined in order to introduce the combined application of POLIPHON in synergy with continuous P-MPL measurements for the separation of, in particular, Saharan dust, fire smoke and pollen particles from other aerosols mixed with them. Those selected dust, smoke and pollen cases occurred on 5 July, 23 May and 23 March 2016, respectively. HYSPLIT backtrajectory (Hybrid Single Particle Lagrangian Integrated Trajectory model Version 4 developed by the NOAA's Air Resources Laboratory (ARL); Draxler and Hess, 1998; Stein et al., 2015, Rolph et al., 2017) analysis is used to confirm the presence of dust and smoke over BCN for each particular case. HYSPLIT backtrajectories are calculated for those days ending over BCN at given altitudes and several times in relation with the results obtained and discussed later in **Section 3** for the dust and smoke cases.

The 5-day backtrajectory analysis indicates Saharan air masses arriving at high altitudes (> 2000 m a.g.l.) on 5 July 2016 only before 12:00 UTC, North Atlantic air masses are simultaneously arriving at lower heights (see **Fig.1**, a-c panels); during the time period after 12:00 UTC, air masses at all altitudes are mostly coming from North Atlantic and central Spain regions (see **Fig. 1**, d-f panels), but not from Saharan desert. On the other hand, smoke plumes detected on 23 May 2016 over BCN seem to be arriving from North America fires using 10-day backtrajectories; depending on the altitude and time of the arrival, air masses are coming from either Canada and USA areas carrying fine biomass burning particles or Artic region with larger aerosols in comparison with those smoke particles (see **Fig. 1**, g-l panels). The pollen case was selected in the period March-April as the day with the highest peak of daily pollen concentration. Such a peak occurred on 23 March 2016 and the most abundant taxon was *Platanus*. Belmonte (2016) counted a near-surface concentration of around 1700 grains of *Platanus* taxon per cubic meter in downtown Barcelona on 23 March 2016. This value is close to the daily values found in the pollination event of March 2015 also in Barcelona described by Sicard et al. (2016) as particularly strong in terms of pollen concentration. These results will be discussed in detail together with those obtained for each aerosol case in **Section 3**.

2.2 Polarized Micro-Pulse lidar (P-MPL) system

The polarized Micro-Pulse lidar system (P-MPL v. 4B, Sigma Space Corp.) acquires vertical aerosol profiles with a relatively high frequency (2500 Hz) using a low-energy (~ 7 µJ) Nd:YLF laser at 532 nm. The P-MPL acquisition settings follow the NASA/MPLNET requirements of 30 s integrating time and 15 m vertical resolution. Polarization capabilities rely on the collection of two-channel measurements (i.e., the signal measured in the so-called relative 'co-polar' and 'cross-polar' channels of the instrument, denoted as $P_{co}(z)$ and $P_{cr}(z)$ signals, respectively; see Sigma Space Corp. Manual, 2012, for more details). By adapting the methodology described in Flynn et al. (2007), the parallel and perpendicular P-MPL range-corrected signals (RCS, also called Normalized-Relative-Backscatter signals, NRB), represented as $P^{||}(z)$ and $P^{\perp}(z)$, respectively, can be expressed in terms of those P-MPL co- and cross-channel signals, $P_{co}(z)$ and $P_{cr}(z)$, respectively, as (hereafter, the dependence with height is omitted for simplicity)

$$P^{||} = P_{co} + P_{cr}, \tag{1}$$

and

$$P^{\perp} = P_{cr} \tag{2}$$

Then, the total RCS, P, can be expressed as

$$P = P^{||} + P^{\perp} = P_{co} + 2\,P_{cr}. \tag{3}$$

Final corrected P, $P^{||}$ and $P^{\perp}$ are obtained using the procedure described in Campbell et al. (2002) and Welton and Campbell (2002). The linear volume depolarization ratio, δ^V, in a classical sense (Sassen, 1991), can be defined as

$$\delta^V = \frac{P^{\perp}}{P^{||}}. \tag{4}$$

Then, the linear volume depolarization ratio δ^V for a MPL system (Flynn et al., 2007) can be easily expressed as

$$\delta^V = \frac{P_{cr}}{P_{co}+P_{cr}}. \tag{5}$$

In order to increase the signal-to noise ratio (SNR), both $P^{||}$ and $P^{\perp}$ are hourly-averaged signals in this work. However, higher uncertainties are found for daytime measurements due to the SNR decrease. Relative uncertainties estimated for the main parameters as derived from P-MPL measurements are shown in **Table 1** (references included).

The particle linear depolarization ratio δ_p is calculated by the procedure shown in Cairo et al. (1999), and expressed as

$$\delta_p = \frac{R \times \delta^V \times (\delta_{mol}+1) - \delta_{mol} \times (\delta^V+1)}{R \times (\delta_{mol}+1) - (\delta^V+1)}, \tag{6}$$

where R is the backscattering ratio ($R = \frac{\beta_m + \beta_p}{\beta_m}$), β_m and β_p are the molecular and particle backscatter coefficients, respectively, and δ_{mol} is the molecular depolarization ratio. Optical filters of the P-MPL receiving system presents a spectral band lower than 0.2 nm (Sigma Space Corp. Manual, 2012), producing a temperature-independent δ_{mol} of 0.00363 according to Behrendt and Nakamura (2002). The particle backscatter coefficient β_p is obtained by applying the Klett-Fernald (KF) algorithm (Fernald, 1984; Klett, 1985) to P ($= P^{||} + P^{\perp}$) profiles obtained from P-MPL measurements in synergy with simultaneous sun-photometer measurements that provide ancillary data of the Aerosol Optical Depth (AOD). Hence, a vertically-averaged lidar ratio (LR, extinction-to-backscatter ratio, denoted as S_a) can be also estimated by using this KF iterative approach in P-MPL measurements, since the LR value varies in each iteration, reaching the convergence once the relative difference between the lidar-derived height-integrated particle extinction profile τ^{MPL} ($= \sum_z \sigma_p(z) = \sum_z [S_a \times \beta_p(z)]$) and the AERONET AOD is lower than a given convergence factor (see Córdoba-Jabonero et al., 2014, for more details of this iterative convergence method applied to specific MPL measurements). In this study, a convergence factor of 1 % is applied (relative uncertainties found for S_a are 5-10 %, see **Table 1**). AERONET V2 inversion Level 1.5 data were used for all the aerosol cases due to the unavailability of the almucantar-derived data from V3 inversion at any level and those scarce data from V2 at Level 2.0. Hence, the threshold limitation of AOD > 0.4 does not apply.Both AOD and the Ångström exponent (AEx) together with other AERONET parameters used in this work were also hourly-averaged in order to coincide with the 1-h averaging applied to P-MPL measurements.

2.3 POLIPHON method

2.3.1 General features

The POLIPHON (POlarization-LIdar PHOtometer Networking) method was developed at the Leibniz Institute for Tropospheric Research (TROPOS, www.tropos.de) for application in polarization-lidar measurements in order to separate the optical properties (backscatter, extinction) of aerosol mixtures into their components with clearly different particle depolarization ratios. POLIPHON can run two ways: as 1-step retrieval (POL-1 approach hereafter) or in 2 steps (POL-2 approach hereafter), retrieving the separation of two or three aerosol components, respectively. A complete description of the POLIPHON discrimination technique can be found in Mamouri and Ansmann (2014). In particular, the POL-1 approach has been successfully applied for separation of dust from biomass burning smoke particles (Tesche et al., 2011; Ansmann et al., 2012), and volcanic ash aerosols from other fine particles (Ansmann et al., 2012; Sicard et al., 2012). The POL-2 approach has been used for partition of dust coarse and fine components and their discrimination from other non-dusty aerosols (marine, anthropogenic pollution) (Mamouri and Ansmann, 2017).

In this work, as stated before, the separation of the optical properties of dust, smoke and pollen particles from their mixtures with other aerosols is performed by applying POLIPHON to P-MPL measurements. The POL-1 approach (2-component separation) is used for the selected smoke and pollen cases on 23 May 2016 and 23 March 2016, respectively, over BCN, in order to discriminate the smoke (SM) signature from other non-smoke (NS) aerosols, and the pollen (PL) particles from other local background aerosols (BA). The dust case observed on 5 July 2016 is examined to present the separation into three components: dust coarse (Dc), dust fine (Df) and non-dusty (ND) aerosols. However, particularly for this case, instead of the POL-2 approach only, a combined version of POLIPHON using together both POL-1 and POL-2 approaches (namely POL-1/2) is applied (Mamouri and Ansmann, 2017). A more detailed description of this POL-1/2 retrieval, and its use in this work, is shown in **Section 2.3.2**.

In general, one of the constraints of POLIPHON is that it is based on the appropriate selection of the linear depolarization ratio for each 'pure' (not mixed) type of specific aerosols. **Table 2** shows the particular δ_i values assumed for each specific (i) aerosol component. In particular, in the dust case $i = 1$ is denoted for total dust (DD), and 2 for non-dust (ND) by using POL-1, and $i = 1$ for dust coarse (Dc), 2 for dust fine (Df), and 3 for non-dust (ND) by using POL-2. In the smoke case, $i = 1$ stands for smoke (SM), and 2 for non-smoke (NS) by using POL-1. In the pollen case, $i = 1$ is for pollen (PL), and 2 for local background aerosols (BA), which are likely a mixture of small pollution particles mostly present in the urban environment of Barcelona city, by using POL-1. After separation of the different aerosol components, the respective extinction coefficients are calculated by assuming LR values typical for each aerosol type: 55 sr for dust (Dc and Df components) (Mamouri and Ansmann, 2014), 70 sr for smoke plumes (Groβ et al., 2013), and 50 sr for pollen particles (Sicard et al., 2016).

The backscatter fraction for each aerosol component is presented along the day, as expressed in terms of the relative ratio between the specific height-integrated backscatter coefficient for each aerosol component, $\overline{\beta_i}$, and the total (sum of all the components) height-integrated particle backscatter coefficient, $\overline{\beta_p}$, i.e., the $\frac{\overline{\beta_i}}{\overline{\beta_p}}$ ratio (%), as calculated from the continuous 24/7 P-MPL measurements.

2.3.2 POL1/2 approach applied to the dust case: combined POL-1 and POL-2 versions

245 In dusty events, POL-1 is used to separate dusty (DD) from non-dusty (ND) aerosols. In contrast, POL-2 is a 2-step approach used to first (step 1) separate Dc particles from the total fine mode (Df + ND) (ND are assumed to be only fine aerosols as composed mostly of small pollution particles, since AODs are large enough for neglecting the marine impact), and then (step 2) that fine contribution is separated into Df and ND particles (see more details in Mamouri and Ansmann, 2014). In the overall POL-2 procedure, the depolarization ratio for the total fine (Df+ND) mixture (i.e.,

250 the residual fine depolarization ratio), δ_{Df+ND}, must be either assumed or known. In our case, δ_{Df+ND} can be estimated by a combined algorithm that uses both POL-1 and POL-2 versions (POL-1/2), as also reported by Mamouri and Ansmann (2017). In particular, the statement that the backscatter coefficient profiles obtained from the POL-1 retrieval for the DD (Dc+Df) component, $\beta_{DD}(z)|_{POL-1}$, is identical to the sum of the backscatter coefficient profiles for the dust coarse (Dc) and dust fine (Df) retrieved independently by the POL-2 version (i.e., $\beta_{Dc}(z)|_{POL-2}$ and

255 $\beta_{Df}(z)|_{POL-2}$, respectively) must be fulfilled. That is,

$$\beta_{DD}(z)|_{POL-1} = \beta_{Dc}(z)|_{POL-2} + \beta_{Df}(z)|_{POL-2}. \tag{7}$$

For that purpose, first, $\beta_{DD}(z)|_{POL-1}$ profiles are derived. Then, a set of both $\beta_{Dc}(z)|_{POL-2}$ and $\beta_{Dc}(z)|_{POL-2}$ are obtained for several δ_{Df+ND} values ranging between the specific depolarization ratios of Df particles (δ_{Df}=0.16) and ND aerosols (δ_{ND}=0.05) (see **Table 2**). Those δ_{Df+ND} are iteratively introduced with steps of 0.01 in the POL-2

260 approach point-to-point along the whole profile in order to obtain an optimal $\delta_{Df+ND}(z)$ profile, which must satisfy that the two terms of the equality in **Eq. (7)** are equal at each z-point. For instance, the minimal value obtained for the root square differences, Δ, between both terms in **Eq. (7)** at a given z,

$$\min\{\Delta(z)\} = min\left\{\sqrt{\left[\beta_{DD}(z)|_{POL-1} - (\beta_{Dc}(z)|_{POL-2} + \beta_{Df}(z)|_{POL-2})\right]^2}\right\}, \tag{8}$$

is used as proxy in that iteration process. Hence, once those $min\{\Delta\}$ are achieved for a given δ_{Df+ND} along the whole

265 profile, the optimal vertical $\delta_{Df+ND}(z)$ profile is determined. Moreover, since $\delta_{Df+ND}(z)$ is defined in a good approximation as

$$\delta_{Df+ND}(z) = \delta_{Df} \times \gamma(z) + \delta_{ND} \times (1 - \gamma(z)), \tag{9}$$

where $\gamma(z)$ and $(1-\gamma(z))$ are, respectively, the fraction of each Df and ND components as contributed to the total fine (Df+ND) mode mixture, this contribution of each aerosol fine component to the total fine mode can also be estimated

270 with height and $\gamma(z)$ is thus determined.

Once the profile of δ_{Df+ND} (and γ) is optimally determined , the total particle backscatter coefficient profiles $\beta(z)$ can be separated into all three components (β_{Dc}, β_{Df} and β_{ND}) for the dust case by applying POL-2 (step 2) retrieval (see Mamouri and Ansmann, 2014, for more details). Hence, their relative contribution (i.e., the $\frac{\overline{\beta_i}}{\overline{\beta_p}}$ ratio, %) can be also derived.

275 For comparison, a columnar δ^c_{Df+ND} value is also calculated using the same POLIPHON procedure as described before, but the minimum of the root mean square differences, $\tilde{\Delta}$, between both terms in **Eq. (7)**,

$$\min\{\tilde{\Delta}\} = min\left\{\sqrt{\frac{\left[\sum_z\left[\beta_{DD}(z)|_{POL-1}-(\beta_{Dc}(z)|_{POL-2}+\left.\beta_{Df}(z)\right|_{POL-2})\right]^2\right]}{n}}\right\}, \qquad (10)$$

is used instead as the proxy applied in the iterative retrieval (n stand for the number of z-points along the overall profile). For instance, **Figure 2** shows the particle backscatter coefficients profiles as obtained from either POL-1 (β_{DD} and β_{ND}) or POL-1/2 (β_{Dc}, β_{Df}, being $\beta_{Dc} + \beta_{Df} = \beta_{DD}$, and β_{ND}) approaches at two times (02:00 and 16:00 UTC) on 5 July 2016, using both the optimal $\delta_{Df+ND}(z)$ profile (**Fig. 2a**), and the columnar δ_{Df+ND}^c (**Fig. 2b**). Discrepancies are observed in both the dust and non-dust components by using a single columnar δ_{Df+ND}^c value instead of the optimal $\delta_{Df+ND}(z)$ profile. For comparison between **Fig. 2a** and **2b**, differences are clearly found in β_{ND} at 02:00 UTC, picked at around 4.5 km height, as derived from either POL-1 or POL-1/2, in addition to those found for β_{DD} in comparison with β_{Dc} and β_{Df} (particularly evident at 16:00 UTC, with $\beta_{DD} \ll \beta_{Df}$ between 1 and 2 km height) (see **Fig. 2b**). These results highlight that the use of a height-resolved δ_{Df+ND} improves the retrieval. Indeed, the use of a single columnar (no height-resolved) δ_{Df+N}^c (and γ^c) in the retrieval can be inadequate due to the plausible variability of the relative fraction of Df particles to the total fine (Df+ND) mode with height. In particular, this is corroborated looking at the optimal height-averaged $\overline{\delta_{Df+ND}}$ values obtained at 02:00 and 16:00 UTC are, respectively: 0.12 ± 0.04 ($\bar{\gamma} = 66 \pm 32$ %) and 0.09 ± 0.05 ($\bar{\gamma} = 40 \pm 38$ %), in comparison with those columnar δ_{Df+ND}^c values found at 02:00 and 16:00 UTC, respectively: 0.14 ($\gamma^c = 82$ %) and 0.06 ($\gamma^c = 9$ %).

2.4 Extinction-to-mass concentration conversion

2.4.1 General procedure

The conversion from extinction (σ, m^{-1}) to mass concentration (M, g m^{-3}) is performed for each component (i) by means of the so-called Mass Extinction Efficiency (MEE, or also mass-specific extinction coefficient) (k, m^2 g^{-1}) by using the relationship (Ansmann et al., 2012; Córdoba-Jabonero et al., 2016) at each altitude z

$$M_i(z) = \frac{\sigma_i(z)}{k_i}. \qquad (11)$$

The effective MEE (k_{eff}, m^2 g^{-1}), linking the total aerosol extinction from all aerosol components (i.e., AOD) to the Total Mass Concentration (TMC), is given by:

$$k_{eff} = \frac{AOD}{TMC}, \qquad (12)$$

where $TMC = \sum_i \overline{M_i}$ represents the total mass loading in g m^{-2}, with $\overline{M_i}$ the height-integrated mass concentration for each component (i.e., $\overline{M_i} = \sum_z M_i(z)\,\Delta z$, with Δz the height resolution). k_{eff} is a measure of the predominant particle size; k_{eff} values lower and higher than 1.5 m^2 g^{-1} are representative of large and small particles, respectively, as reported by the Optical Properties of Aerosols and Clouds database (OPAC; www.pole-ether.fr). The mass contribution or fraction of each aerosol component is expressed by the relative ratio between $\overline{M_i}$ and TMC (i.e., $\overline{M_i}/TMC$, in %).

Columnar MEE values can be obtained from AERONET data and the particle density (Pd, g cm^{-3}) assumed for each aerosol component examined in this work by using the expression (Ansmann et al., 2012):

$$k_{c,f} = \frac{\tau_{c,f}}{Pd \times VC_{c,f}} = \frac{1}{Pd \times c_{v_{c,f}}}, \tag{13}$$

where $k_{c,f}$ designate the MEE for coarse and fine modes, as denoted by subscripts 'c' and 'f', respectively. Similarly, $VC_{c,f}$ (10^{-12} Mm) and $\tau_{c,f}$ are the AERONET V2 L1.5 volume concentrations and extinction values, respectively, for the coarse and fine modes. $c_{v_{c,f}}$ ($= \frac{VC_{c,f}}{\tau_{c,f}}$) are the corresponding so-called extinction-to-volume conversion factors.

Our strategy is to obtain the actual $c_{v_{c,f}}$ values, and then the $k_{c,f}$ using typical particle densities, from AERONET sun-sky photometer observations performed simultaneously with P-MPL observations, as long as the separated aerosol components can be identified as composed of pure coarse or fine particles. **Table 3** shows the AERONET parameters involved in the extinction-to-mass conversion ($VC_{c,f}$, $\tau_{c,f}$) at selected times for each aerosol case together with those typical particle densities Pd for each aerosol component. In particular, Pd values assumed for each type of aerosols are: 2.60 g cm^{-3} for dust (Ansmann et al., 2012), 1.30 g cm^{-3} for smoke (Reid et al., 2005), 0.92 g cm^{-3} for pollen (*Platanus*) particles (Jackson and Lyford, 1999; Zhang et al., 2014). For the other components, the particle density is obtained from the OPAC database (Hess et al., 1998). A particle density Pd = 1.8 g cm^{-3} is assumed for both the ND and BA components in the dust and pollen cases, respectively, corresponding to background urban aerosols, mostly composed of fine pollution particles. For the NS component in the smoke case, a Pd_{NS} = 2.0 g cm^{-3}, as reported by OPAC for Arctic aerosols, is assumed since the NS signature is found when air masses are coming from the Arctic as indicated by backtrajectory analysis (see **Sect. 2.1**). However, the corresponding c_v and k values must be examined in more detail in the extinction-to-mass conversion procedure for each aerosol case, as explained next.

2.4.2 Dust case

As stated before, POL-1/2 retrieval is applied to separate three components for the dust case (i = Dc, Df and ND). Conversion factors are only reported for coarse and fine mode particles in overall using AERONET data (**Eq. 13**). In this case, the coarse mode is completely composed by Dc particles (the ND component is assumed to be fine aerosols only, see **Sect. 2.3**). Hence, the MEE for Dc particles, k_{Dc}, is easily obtained from

$$k_{Dc} = \frac{\tau_c}{Pd_{Dc} \times VC_c} = \frac{1}{Pd_{Dc} \times c_{v_c}}, \tag{14}$$

with Pd_{Dc} = 2.6 g cm^{-3} for dust. However, MEE for Df particles, k_{Df}, and ND aerosols, k_{ND}, must be determined from the MEE value obtained for the total fine (Df+ND) mode, k_{Df+ND}, that is,

$$k_{Df+N} = \frac{\tau_f}{Pd_{Df+ND} \times VC_f} = \frac{1}{Pd_{Df+ND} \times c_{v_f}}, \tag{15}$$

where Pd_{Df+ND} represents a weighted value of the particle density for the overall fine (Df+ND) mode. Once estimated δ_{Df+ND}, and γ (see **Eq. 9**), Pd_{Df+ND} can be expressed as

$$Pd_{Df+ND} = Pd_{Df} \times \gamma + Pd_{ND} \times (1 - \gamma), \tag{16}$$

where Pd_{Df} and Pd_{ND} are the particle densities assumed for dust (2.6 g cm^{-3}) and non-dust aerosols (1.8 g cm^{-3}), respectively (**Table 3**). Hence, the height-integrated mass concentration for the total fine (Df+ND) mode, $\overline{M_{Df+}}$, can be calculated from

$$\overline{M_{Df+ND}} = k_{Df+ND}^{-1} \times \tau_{Df+ND} = \overline{M_{Df}} + \overline{M_{ND}}, \tag{17}$$

where k_{Df+ND} is calculated from **Eq. 15**, and $\overline{M_{Df}}$ and $\overline{M_{ND}}$ are, respectively, the mass concentrations for Df and ND aerosols (note that these quantities are height-integrated variables, i.e., mass loadings). In particular, $\overline{M_{Df}}$ can be determined by assuming a representative conversion factor c_v for Df particles, since

$$\overline{M_{Df}} = \tau_{Df} \times Pd_{Df} \times c_{v_{Df}}. \tag{18}$$

Mamouri and Ansmann (2017) reported statistical AERONET-based extinction-to-mass conversion factors for dust fine particles $c_{v_{Df}}$ in the interval of 0.21-0.25 ($\pm$ 0.05) 10^{-12} Mm. In this work, this set of values is introduced in the algorithm in order to obtain an optimal $c_{v_{Df}}$ value satisfying the following condition: $\overline{M_{Df}} < \overline{M_{Df+ND}}$, being estimated $\overline{M_{Df}}$ from **Eq. 18**. At the same time, $\overline{M_{ND}}$ is also obtained, since

$$\overline{M_{ND}} = \overline{M_{Df+ND}} - \overline{M_{Df}}. \tag{19}$$

Hence, k_{Df} and k_{ND} (and $c_{v_{ND}}$) are calculated applying, similarly to **Eqs. 13-15**, the following expressions:

$$k_{Df} = \frac{1}{Pd_{Df} \times c_{v_{Df}}}, \tag{20}$$

$$k_{ND} = \frac{\tau_{ND}}{M_{ND}}, \tag{21}$$

and

$$c_{v_{ND}} = \frac{1}{Pd_{ND} \times k_{ND}}. \tag{22}$$

Otherwise, $\overline{M_{Df}} = \overline{M_{Df+ND}}$ (and then, $k_{Df} = k_{Df+ND}$), and $\overline{M_{ND}} = 0$. Finally, the total mass concentration TMC (i.e., mass loading, in g m^{-2}) is obtained from

$$TMC = \overline{M_{Dc}} + \overline{M_{Df+ND}} = \overline{M_{Dc}} + \overline{M_{Df}} + \overline{M_{ND}}. \tag{23}$$

Those AERONET parameters used in the extinction-to-mass conversion together to the particular c_v and k values obtained at some explicit times (see **Table 3**) are in agreement with those reported by other authors (i.e., Mamouri and Ansmann, 2014; 2017) for dust. In addition, k_{ND} values are derived between 2.52 and 2.92 m^2 g^{-1}, similar to those reported by OPAC for urban aerosols (2.87 m^2 g^{-1}), as assumed for the ND component in this work.

2.4.3 Smoke and pollen cases

For both cases, optical properties are separated into two aerosol components by using POL-1 approach. Hence, mass concentrations are derived directly from **Eqs. 11-13** of the general extinction-to-mass conversion procedure using AERONET data, satisfying that each component is composed mostly of either coarse or fine mode particles, as described in **Section 2.4.1**.

In particular, the smoke (SM) component is composed of fine biomass burning particles, and the coarse mode is associated to the non-smoke (NS) component by assuming particles larger than smoke coming from the Arctic area. For instance, a $k_{SM} = 4.5 \pm 1.4$ m^2 g^{-1} is derived for fine smoke particles at 06:00 UTC (see **Table 3**). This value is in

good agreement with that reported for Canadian forest fire smoke aerosols (Ichoku and Kaufman, 2005; Reid et al., 2005). However, a rather lower MEE value is obtained for the coarse mode NS particles ($k_{NS} = 2.4 \pm 0.5$ m^2 g^{-1}) at the same time. In the pollen case, PL particles are predominantly large particles in comparison with the fine (and less depolarizing) component corresponding to local background aerosols (BA), that are assumed composed of small 375 polluted particles of urban origin (marine contribution is neglected, as stated in **Sect. 2.**). For instance, a $k_{PL} = 2.3 \pm 0.1$ m^2 g^{-1} is obtained for pollen particles at 15:00 UTC, when pollination event is enhanced, as described later in **Section 3.3**.

Table 3 shows the derived MEE values (k, m^2 g^{-1}) at selected times by using the corresponding c_v factors and the assumed particle densities (Pd, g cm^{-3}) for each component. Particular similarities and discrepancies found from those 380 assumptions will be discussed in more detail in **Section 3**.

3 Results

3.1 Dust case

A dusty event occurred over BCN on 5 July 2016, which was mostly intense before 12:00 UTC as confirmed by AERONET data with moderate AOD and AEx < 0.5 values together with HYSPLIT backtrajectory analysis (**Sect.** 385 **2.1**). The separation into three components (Dc, Df and ND) of dusty mixtures using the synergy of hourly-averaged P-MPL measurements and POL-1/2 retrieval was performed along the day. Prior using POL-1/2, vertical profiles of the total particle backscatter coefficient (β_p), as derived from the KF algorithm (if the KF retrieval is feasible, estimated LR values are discussed later), and the linear particle depolarization ratio (δ_p) are obtained along the day. Then, the corresponding vertical profiles of the backscatter coefficients for each specific component (β_i, i = Dc, Df, 390 ND) were retrieved by using POL-1/2 (**Sect. 2.3.2**). The three specific depolarization ratios selected for each pure aerosol component (δ_i, i = Dc, Df, ND), required for the POL-1/2 retrieval, are shown in **Table 2**. As mentioned before, height-integrated values of all these backscatter coefficient profiles ($\overline{\beta_p}$, and the three $\overline{\beta_i}$ for each component) are calculated along the 24 hours of the day (if the KF retrieval is feasible) to obtain the daily temporal evolution of the optical contribution for each aerosol component in terms of their specific relative ratio $\frac{\overline{\beta_i}}{\overline{\beta_p}}$ (in %). Regarding the 395 height-integrated mass concentration ($\overline{M_i}$, i = Dc, Df, ND; **Sect. 2.4**), the daily evolution of specific mass contribution ratio (i.e., the relative ratio $\frac{\overline{M_i}}{TMC}$, in %), is also calculated for each aerosol component (note that height-integrated mass concentrations represent the mass loading, expressed in g m^{-2}). For simplicity, the same notation is used for mass concentration and mass loading.

Figure 3 shows the daily evolution of the specific (a) optical and (b) mass relative contribution for each aerosol 400 component along the day. A high loading of large particles with peaks of 78 % for β_{Dc} and 98 % for M_{Dc} was obtained in the time interval before 12:00 UTC. These peaks drop to minimums of 9 and 43 %, respectively, after that time. Here, the optical contribution of the total dust (Dc+Df) varies between 17 and 46 %, while the mass contribution ratio varies between 56 and 98 %. In terms of mean TMC (dust loading), values of 0.6 ± 0.1 and 0.2 ± 0.1 g m^{-2} are estimated,

respectively, at those time intervals before and after 12:00 UTC. The last one represents a TMC of 34 % with respect to that found in the previous period of the day. Specific $\overline{M_l}$ and TMC at given times are shown in **Table 4**. Therefore, two differentiated dusty scenarios with an intense and weak dust impact are clearly observed along the day.

These results are related to the mean MEE values found for dust particles: $k_{Dc} = 0.5 \pm 0.1$ m^2 g^{-1} and $k_{Df} = 1.7 \pm 0.2$ m^2 g^{-1} as obtained for Dc and Df particles, respectively. These quantities are within and close to the range of values representative, respectively, for coarse- and fine-dominated dust particles, as reported by the OPAC database (www.pole-ether.fr): 0.16-0.97 m^2 g^{-1} (dust coarse) and 2.3-3.1 m^2 g^{-1} (dust fine). Higher MEE values are obtained for the ND component ($k_{ND} = 3.1 \pm 1.3$ m^2 g^{-1}, in daily average), indicating much smaller particles, and close to that value of 2.87 m^2 g^{-1} reported by OPAC (Hess et al., 1998) for urban aerosols (note that fine polluted aerosols with urban origin were assumed for the ND component). For comparison, the corresponding mean conversion factors c_v obtained for Dc and Df particles are, respectively, $c_{v_{Dc}} = 0.8 \pm 0.3$ 10^{-12} Mm and $c_{v_{Df}} = 0.24 \pm 0.02$ 10^{-12} Mm, values that are in good agreement with other reported values (i.e., Mamouri and Ansmann, 2017).

AERONET AOD and AEx values provided along the day (night-time data are assumed equal to the first and last daytime values in each case) also confirm these results (see **Fig. 3a**). In particular, AEx is close to 0.5 (coarse particle predominance) and higher than 1.5 (fine particle prevalence), respectively, before and after 12:00 UTC. Regarding LR values as derived from the KF algorithm (**Fig. 3a**, right axis), a daily mean $S_a = 42 \pm 15$ sr is obtained. No significant differences are found between LR values obtained for those intense and weak dusty periods of the day, and just a certain variability is observed along the day as modulated by the dust loading, as expected.

In order to illustrate the vertical distribution of dust particles, **Figure 4** shows an example in terms of the profiles of both the particle backscatter coefficients (total β_p, and β_{Dc}, β_{Df} and β_{ND}, left panels) and the linear depolarization ratios (volume δ^v and particle δ_p, right panels) of both aerosol scenarios: 1) when the dust event presents a high incidence as occurred for instance at 02:00 UTC (**Fig. 4a**); and 2) after the dust particles are almost completely removed (i.e., situation observed at 16:00 UTC, see **Fig. 4b**). These scenarios are also indicated in **Figure 3** by black arrows. An enhanced dust impact is observed in **Fig. 4a** (02:00 UTC) due to a high amount of Dc particles confined in a layer located between 2 and 5 km height (red line in **Fig. 4a**). Contrarily, **Fig. 4b** (16:00 UTC) shows a rather weaker dust incidence from the ground up to 4 km height mostly due to a low loading of both Dc and Df particles (red and green lines, respectively, in **Fig. 4b**). Indeed, according to HYSPLIT backtrajectories (**Sect. 2.1**), no Saharan origin of air masses is observed after 12:00 UTC (see **Fig. 1**, d-e panels).

AERONET AOD and AEx and KF-derived LR values for those different dusty scenarios are also included in **Table 2**. In particular, a $S_a = 50 \pm 10$ sr is retrieved at 02:00 UTC that is within the typical LR range determined for dust. Meanwhile a lower value ($S_a = 29 \pm 6$ sr) is found at 16:00 UTC, when a rather weaker dust incidence occurs. Moreover, δ_p shows values close to the linear particle depolarization ratio for pure Dc particles (δ_{Dc}=0.39) for the first aerosol scenario (**Fig. 4a**, centre panels), and slightly lower than 0.16 (δ_{Df} for pure dust fine particles) for the second one (**Fig. 4b**, centre panels). In addition, the δ_{Df+ND} profiles for those times are also shown in **Figure 4** (right panels) in order to examine the corresponding variability of the Df contribution to the particle fine mode with height: δ_{Df+ND} is greater than 0.10, indicating that the Df fraction within the fine mode is larger than 45.5 %, at altitudes

440 higher than 1.5 and around 4.0 km height, respectively, for those two dusty situations (**Fig. 4a** and **4b**, respectively), in correspondence with the backscatter profiles; otherwise, Df fraction is reduced (< 40 %) at lower heights. In these two particular cases (**Fig. 4**), the derived MEE values are close to the typical ranges for Dc (k_{Dc}: 0.5-0.6) and Df (k_{Df}: 1.5-2.0) aerosols (see **Table 3**).

3.2 Smoke case

445 Smoke plumes were observed over BCN station on 23 May 2016. The two principal areas that air masses are arriving from are North America and the Arctic, as reported by HYSPLIT backtrajectory analysis for that day at several times (see **Fig. 1**, g-l panels). The smoke origin is likely from forest fires occurred in North America (as stated in **Sect. 2.1**). Hence, the smoke case is examined as a mixture of two components: fine biomass burning particles (SM for smoke) from Canada and USA fires, and another particle type larger than smoke coming from the Arctic region (hereafter,

450 referred to as non-smoke aerosols, NS). Their vertical separation is achieved using POL-1 retrieval (2-component separation), as described in **Sect. 2.3** and **2.4**. Both the particular backscatter coefficients and mass concentrations are retrieved for each component. In particular, the arrival of smoke plumes over BCN is mostly at altitudes above the boundary layer (BL); hence, this case is focused only on those tropospheric features above the BL, thus disregarding aerosols from other plausible local background BL sources.

455 Like for the dusty case, **Figure 5** shows the relative fractions of each SM and NS components in terms of the backscatter coefficient and the mass concentration along the day. Those k values together with the c_v factors at selected times are shown in **Table 3**, as well as the Pd values assumed: 1.30 g m^{-3} for SM and 2.0 g m^{-3} for NS aerosols (see **Sect. 2.4**). Since values of δ_p higher than 0.1 are found at given altitudes along the day, a high-limit value of the particle linear depolarization ratio for smoke, δ_{SM} of 0.15, is assumed. This rather high δ_{SM} value is typical for smoke

460 particles mixed with dust (Tesche et al., 2011; Groβ et al., 2013), as one would expect δ_{SM} < 0.10 for pure biomass burning particles (Müller et al., 2005; Groβ et al., 2013). In addition, AERONET AEx varies between 1.25 and 1.55 before 12:00 UTC (see **Fig. 5a**), indicating rather moderate AEx values as compared to higher fresh smoke values (~ 2.00), as measured by Sicard et al. (2011) also in Barcelona. Hence, the value of δ_{SM}=0.15 reflect a mixing state of biomass burning particles, but not necessarily with dust. For the other, less depolarizing, NS component, a δ_{NS}=0.05

465 is applied. Those particle linear depolarization ratio values assumed for SM and NS are shown in **Table 2.**

In general, smoke particles are detected during almost all the day, representing approximately 40-60 % of the total height-integrated aerosol backscatter. However, a sharp $\frac{\overline{\beta_{SM}}}{\beta_p}$ decrease from those values to around 4 % is observed at 15:00 and 16:00 UTC, which coincides with the 47 % decrease found for AEx (see **Fig. 5a**). Since lower AEx values are usually associated with the predominance of large particles and/or the fine mode decrease, these results are in

470 agreement with that observed reduction of fine biomass burning particles during the same time interval. At those same times, the TMC reaches high values (0.26 ± 0.06 g m^{-2}, in average) with respect to the daily mean TMC background of 0.05 ± 0.03 g m^{-2}. This is likely due to the major contribution of larger NS aerosols, meanwhile fine SM particles represent only a 3-7 % of TMC at the same times. In particular, the daily mean $\overline{M_{SM}}$ is 0.017 ± 0.008 g m^{-2}, representing 2.7 % of the mean TMC found for the dust case. Regarding KF-derived LR values (see **Fig. 5a**, right axis), a daily

mean S_a = 56 ± 23 sr is obtained. That value is lower as compared to typical LR of 70 sr for smoke (i.e., Groβ et al., 2013, and references therein), which together with the large relative deviation (42 %) indicates a high aerosol variability along the day as expected due to the singular arrival of air masses in height and time, and hence the particular vertical aerosol mixing found with the smoke particles.

Regarding the vertical structure, **Figure 6** shows examples of two different aerosol scenarios observed on the day: 1) a well-defined smoke layer is observed, for instance, between 6 and 7.5 km height with a certain mixing with NS aerosols at 06:00 UTC (see **Fig. 6a,** red line); and 2) the smoke signature can be detected highly mixed with NS aerosols along the atmospheric profile (i.e., situation observed at 14:00 UTC, see **Fig. 6b**). These both scenarios are also indicated in **Figure 5** by black arrows. Indeed, the mean S_a values of 70 ± 19 and 35 ± 9 sr found, respectively, before and after 12:00 UTC reflect that the smoke signature detected during the first of those time periods of the day presents a lower mixing with other aerosols than that observed later. Additionally, in average, the mean height-integrated mass concentration for smoke is also obtained in those two different scenarios: $\overline{M_{SM}}$ = 0.014 ± 0.002 and 0.022 ± 0.009 g m^{-2} are found, respectively, for those time intervals. Those values represent 2.2 and 3.4 %, respectively, of the TMC found for the intense dust period. **Figure 6a** clearly shows a smoke layer between 6 and 7.5 km height, also mixed with a certain NS contribution, exhibiting δ_p values of 0.15 and higher. In addition, a smaller SM layer of about 300 m thickness is also found below at around 5.2 km height with rather higher δ_p than 0.15, and another layer is observed between 3 and 4 km height corresponding to the presence of NS aerosols with a δ_p slightly higher than 0.05. The fraction of smoke particles is around 50 % out of total backscatter (see **Fig. 5a**) with a height-integrated mass concentration for smoke $\overline{M_{SM}}$ = 0.012 ± 0.002 g m^{-2}, representing 2 % out of the mean TMC during the intense dusty event (see **Table 4**).

Later in the day at 14:00 UTC, both SM and NS particles are found along all the profile, with δ_p values close to 0.15, mainly between 4.0 and 4.5 km height. In addition, a single NS layer is also clearly observed, peaking at 2.5 km height, with δ_p values decreasing down to 0.05 (see **Fig. 6b**). These results agree with the δ_p value selected for NS aerosols (δ_{NS}=0.05, see **Table 2**). At this time, a $\overline{M_{SM}}$ = 0.023 ± 0.001 g m^{-2}, being 4 % out of the mean TMC for the intense dusty episode, is obtained. Particular LR values for those times shown in **Figure 6** are also included in **Table 2**: S_a = 81 ± 16 sr is retrieved at 06:00 UTC that is within the typical LR range determined for smoke, while a lower LR (S_a = 45 ± 9 sr) is found at 14:00 UTC, as expected. Particular MEE values derived for smoke particles, k_{SM} = 4.5 ± 1.1 and 1.9 ± 0.4 m^2 g^{-1} are obtained, respectively, at 06:00 and 14:00 UTC. These results would indicate that smoke plumes detected in the first scenario are predominantly composed of relatively pure fine biomass burning particles, with similar MEE values to those reported for Canadian boreal forest fire aged smoke particles (Ichoku and Kaufman, 2005; Reid et al., 2005). However, those observed in the second one would represent a mixed state of smoke particles with an enhanced coarse mode, thus decreasing their MEE. All those values are shown in **Tables 3** and **4**.

These results are corroborated by a more detailed analysis of the backtrajectories ending over BCN on 23 May 2016 (selected heights and times of their arrival are shown in **Fig. 1**). In particular, air masses arriving at 06:00 UTC are carrying out smoke particles from Canada and USA fires at altitudes higher than around 4500 m a.s.l. (see **Fig. 1**, h-i panels), while Arctic air masses arrive at lower heights (see **Fig. 1**, g panel). Later on, a smoke signature observed at

14:00 UTC is distributed from altitudes higher than around 3000 m a.s.l. height up (**Fig. 1**, k-l panels), and the NS layer identified at around 2500 m height (see **Fig. 6b**) actually corresponds to air masses coming from the Arctic (see **Fig. 1**, j panel).

3.3 Pollen case

515   The pollination period (i.e., the enhanced formation/presence of pollen particles) in Barcelona is from local sources predominately occurring in March from the more abundant species, such as the *Pinus* and *Platanus* trees (Sicard et al., 2016a). In this case, a pollen episode occurred on 23 March 2016, corresponding to a high pollination event observed over BCN (Belmonte, 2016). As for the smoke case, POL-1 retrieval is used to separate pollen (PL) particles from background (BA) aerosols. These BA are supposed to be mostly composed of urban fine polluted particles, and

520   their exact origin, whether they are local or not, is not relevant since they do not depolarize and cannot be mistaken for highly depolarizing pollen particles. This is also the reason why HYSPLIT backtrajectories were not calculated.. Particle linear depolarization ratios for 'pure' PL, δ_{PL}=0.40, and BA, δ_{BA}=0.05, aerosols are shown in **Table 2**, as well as those k (and c_v) values are in **Table 3**. The relative fractions of each aerosol component in terms of the backscatter coefficient and the mass concentration are also calculated along the day.

525   Pollen signature is clearly observed from 10:00 UTC on, as shown in **Figure 7** by the increase of their relative fraction $\frac{\overline{\beta_{PL}}}{\overline{\beta_p}}$, with a maximum around 30 % between 12:00 and 16:00 UTC. The coincident increase of AEx (see **Fig. 7a**) is probably associated to the formation of local urban aerosols, which are much smaller as compared to pollen grains. This hypothesis suggests that local urban aerosols dominate the columnar-averaged optical properties. A mean value of S_a = 55 ± 17 sr is obtained during the pollen occurrence, while S_a = 71 ± 17 sr is found for the no pollen detection

530   period. That S_a value for pollen is close to that considered in other works (Sicard et al., 2016a). The fraction of the height-integrated mass concentration for pollen $\overline{M_{PL}}$ with respect to the TMC reaches a maximum of around 40 % at 15:00 UTC. In addition, the TMC evolution is fairly constant with a daily-averaged TMC of 0.029 ± 0.003 g m^{-2}, being that mean $\overline{M_{PL}}$ = 0.007 ± 0.003 g m^{-2}(i.e., 25 % out of TMC) in the 12:00-23:00 UTC interval. For comparison, these TMC levels represent only 1.1 % of the dust TMC during their higher dust incidence, as discussed in **Sect. 3.1**.

535   Regarding the MEE derived for pollen particles, a mean k_{PL} = 2.4 ± 0.8 m^2 g^{-1} is obtained. Sicard et al. (2016a) estimated a k_{PL} = 3.2 m^2 g^{-1} considering an effective radius size of 24 μm for the pollen grains registered during a pollination episode in March 2015 (data not shown). Hence, the k_{PL} value found in this work can be in agreement with that estimated value as long as pollen particles detected in our case are larger than those observed by Sicard et al (2016a), as MEE decreases as particle size increases.

540   In order to display the vertical distribution for this case, profiles of the particle backscatter coefficients and both the volume and particle linear depolarization ratios are shown in **Figure 8** (see legend inside). For instance, the vertical distribution is shown at 10:00 UTC, when no pollen particles are significantly detected (**Fig. 8a**), with low δ_p values close to 0.05 from surface up to around 1 km height and slightly increasing from that altitude up. This is likely due to uplifted particles. In comparison, the situation occurred later on the day (i.e., that observed at 15:00 UTC, **Fig. 8b**),

545   the amount of pollen clearly enhances: δ_p increases, reaching higher values between 0.10 and 0.15, and pollen particles

are mostly confined up to 1.5 km height from the surface. These two scenarios are also indicated in **Figure 7** by black arrows. The corresponding mass loading for pollen $\overline{M_{PL}}$ at this time is 0.011 ± 0.003 g m^{-2} (see **Table 4)**.

4 Conclusions

The synergetic use of the POLIPHON (POlarization-LIdar PHOtometer Networking) retrieval with the MPLNET (Micro-Pulse Lidar NETwork)/P-MPL (polarized MPL) measurements is introduced for the first time in order to separate dust (both coarse Dc, and fine Df, modes) and biomass burning smoke (SM) particles from their mixtures with other aerosols (namely, non-dust ND, and non-smoke NS aerosols). In addition, a case study of pollen (PL) mixed with local urban background aerosols (BA) is also examined. In all cases, the particle linear depolarization ratio for each aerosol 'pure' component is a relevant constraint in POLIPHON retrievals. The separation of aerosol mixtures into their particle components is performed for different depolarising particles. In particular, typical linear depolarization ratios found in the literature are assumed for each pure aerosol component: 0.39, 0.16 and 0.05, respectively, for Dc, Df and ND; 0.15 and 0.05, respectively, for SM and NS; and 0.40 and 0.05, respectively, for PL and BA.

In this work, a reasonable performance is achieved by obtaining the relative optical and mass contributions of each aerosol component along the day as based on P-MPL continuous 24/7 observations carried out in Barcelona (NE Spain). Three case studies observed on 5 July, 23 May and 23 March 2016 are examined, respectively, for dust, smoke and pollen occurrences. In particular, the POLIPHON 1-step version (POL-1: separation into two components) is applied for the smoke and pollen cases. In order to illustrate the 3-component separation for the dust case, a combined algorithm using both the POLIPHON 1-step (POL-1) and 2-step (POL-2) versions (namely POL-1/2) is described in more detail. In addition, both the vertical and columnar particle depolarization ratio for the total fine (Df+ND) mode, δ_{Df+ND}, and correspondingly both the vertical and columnar fraction of Df particles to the total fine (Df+ND) mode, are also estimated using the POL-1/2 retrieval (the a priori assumption of those variables is thus avoided).Minimal differences in the particle backscatter coefficient, β, for each dusty and non-dusty component are found as obtained from either POL-1 or POL-1/2 approaches, as long as a vertical depolarization ratio for the total fine (Df+ND) mode $\delta_{Df+ND}(z)$ is regarded. Otherwise, the use of a single columnar, no height-resolved, δ_{Df+ND}^c is inadequate due to the plausible Df variability, with respect to the total fine mode, with height.

The extinction-to-mass conversion procedure is described in terms of the Mass Extinction Efficiency (MEE: k, m^2 g^{-1}), a parameter associated to the size of the particles. The MEE is estimated for each aerosol component by using the corresponding conversion factors as calculated from AERONET data (volume concentrations and extinctions for the coarse and fine modes), as reported at simultaneous times with P-MPL measurements, and the particles densities assumed for each type of aerosol. In addition, the effective MEE (k_{eff}, a measure of the predominant size of those aerosol mixtures) is also retrieved for each aerosol event. Hence, height-integrated mass concentrations (i.e., mass loadings, g m^{-2}) are obtained along the day for each component. In general, the daily evolution of their relative optical and mass contributions, with respect to the height-integrated total backscatter coefficient and total mass concentration (total mass loading) for each aerosol case, is also derived. Due to the variation of the aerosol situation observed for

each case study along the day, different aerosol scenarios can be present, and hence their vertical distribution are examined.

In the dust case occurred on 5 July 2016, a Saharan dust intrusion arrives at BCN during the first part of the day (before 12:00 UTC). Meanwhile a weak dust incidence is observed later on, as also confirmed by AERONET data and HYSPLIT backtrajectory analysis. This is due to the predominance of large particles (Dc component) during this intense dust period of the day. In terms of mean dust mass loading, values of $TMC = 0.6 \pm 0.1$ and 0.2 ± 0.1 g m^{-2} are obtained, respectively, at time intervals before and after 12:00 UTC. This last value just represents a mass loading of 34 % with respect to that found before. In addition, mean MEE values of $k_{Dc} = 0.5 \pm 0.1$ m^2 g^{-1} and $k_{Dc} = 1.7 \pm 0.2$ m^2 g^{-1} are obtained for Dc and Df particles, respectively. These quantities are within and close to the range of values representative of coarse- and fine-dominated dust particles, respectively. AERONET AOD and AEx values reported along the day confirm these results. In particular, AEx is close to 0.5 (coarse particles predominance) and higher than 1.5 (fine particles prevalence), respectively, before and after 12:00 UTC. A mean KF-derived lidar ratio $S_a = 42 \pm 15$ sr is obtained with no significant differences for those two time periods of the day.

Regarding particular aerosol scenarios, a $S_a = 50 \pm 10$ sr is retrieved at 02:00 UTC (within the typical range of lidar ratios defined for dust), meanwhile a lower value ($S_a = 29 \pm 6$ sr) is found at 16:00 UTC when a rather weaker dust incidence occurs. Moreover, δ_p shows values close to the particle linear depolarization ratio for pure Dc particles (0.39) during the intense dusty scenario, and lower than 0.16 (typical for pure dust fine particles) for the weak one, highlighting the prevalence of ND aerosols. In addition, the particle depolarization ratio for the total fine (Df+ND) mode is greater than 0.10, that is, the relative Df fraction within the total fine mode is larger than 45.5 %, at altitudes higher than 1.5 and around 4.0 km height, respectively, for those two particular dusty situations. The derived MEE values are typical for Dc (k_{Dc}: 0.5-0.6) and Df (k_{Dc}: 1.5-2.0) aerosols in those two particular cases.

For a smoke case, air masses arriving over Barcelona (BCN) on 23 May 2016 come from two areas: North America and the Arctic, as reported by HYSPLIT backtrajectory analysis. Fine biomass burning particles originated from fires occurred in Canada and USA, which were likely mixed with other larger than smoke aerosols coming from the Arctic region (non-smoke aerosols, NS). In general, both SM and NS particles were found along all the profile; δ_p values are higher than 0.10 and close to 0.15 when SM particles were mostly detected. Fine smoke particles are observed during almost all the day, representing approximately 40-60 % of the total height-integrated aerosol backscatter coefficient. The mean mass loading for smoke is $\overline{M_{SM}} = 0.017 \pm 0.008$ g m^{-2}, representing 2.7 % out of that mean TMC found for the dust case. However, individual decreases in the relative smoke fractions of both the backscatter coefficient and mass concentration are also observed along the day, coinciding also in time with AEx decreases (as associated to predominance/reduction of coarse/fine particles).

Regarding the vertical structure, two aerosol scenarios are observed along the day: the smoke signature is specially detected at defined layers in the beginning of the daytime, while a vertical SM distribution mixed along with a NS layered structure is observed later on. Mean LR values of $S_a = 70 \pm 19$ and 35 ± 9 sr are found, respectively, before and after 12:00 UTC on that day, showing a lower smoke mixing for the first time interval In addition, the mean mass loading for smoke as obtained in those two different scenarios is $\overline{M_{SM}} = 0.014 \pm 0.002$ and 0.022 ± 0.009 g m^{-2}, respectively (i.e., 2.2 and 3.4 %, respectively, out of the TMC found for the intense dust period). This is likely due to

the singular arrival of air masses in height and time, and hence the particular vertical aerosol mixing found together with the smoke particles over BCN. Corresponding MEE values derived for smoke particles in those two scenarios are $k_{SM} = 4.5 \pm 1.1$ and 1.9 ± 0.4 m^2 g^{-1}, respectively, indicating that smoke plumes detected in the first scenario are predominantly composed of mostly pure fine biomass burning particles, unlike the situation in the second one with a mixed state of smoke particles with an enhanced coarse mode.

In the pollen case occurred on 23 March 2016, the PL signature is clearly observed from 10:00 UTC on, when the relative fraction of the height-integrated backscatter coefficient for pollen enhances, reaching a maximum around 30 % between 12:00 and 16:00 UTC, and δ_p increases with values between 0.10 and 0.15 from the surface up to around 1.5 km height. A mean LR of $S_a = 55 \pm 17$ sr is obtained during the pollen occurrence period. This value is close to that considered by other authors. The relative fraction of mass loading for pollen reaches a maximum of around 40 % at 15:00 UTC, being that mass loading of $\overline{M_{PL}} = 0.011 \pm 0.003$ g m^{-2} (i.e., 1.7 % out of that for dust during their higher incidence). In addition, the mean MEE derived for pollen particles is $k_{PL} = 2.4 \pm 0.8$ m^2 g^{-1}, representing an intermediate value between those reported for Df particles ($k_{Df} = 1.7 \pm 0.2$ m^2 g^{-1}) and for smaller local background urban polluted aerosols ($k_{BA} = 3.4 \pm 0.7$ m^2 g^{-1}). However, the k_{PL} can reach higher/lower values depending on a prevalent smaller/larger size of the pollen grains.

In summary, the vertical separation of aerosol mixtures into their components is achieved using the POLIPHON retrieval in synergy with continuous 24/7 P-MPL measurements together with AERONET data. The methodology, including the extinction-to-mass conversion procedure, is described and applied to several aerosol mixtures case studies. Therefore, vertical optical and mass features are obtained in a daily basis for different climate-relevant aerosols: dust, smoke and pollen particles. It should be noted that the method can be relatively easily applicable to other P-MPLs also within the world-wide NASA/Micro-Pulse Lidar Network (MPLNET), since all those systems present the same instrumental and operating configuration. Hence, the aerosol discrimination can be extended at a global scale. In addition, it can be also adapted to spaceborne lidars with an equivalent configuration (elastic with a depolarization-sensitive channel) such as the ongoing CALIOP/CALIPSO, and the forthcoming ATLID/EarthCARE (future ESA mission to be launched in 2019).

Appendix A. List of acronyms.

Symbol (*) (**)	Parameter	Units
P_{co}, P_{cross}	P-MPL signal channels: co-polar and cross-polar, respectively	a.u.
$P, P^{\|\|}, P^{\perp}$	P-MPL range-corrected signals: total, parallel, perpendicular signals, respectively ($P = P^{\|\|} + P^{\perp} = P_{co} + 2\,P_{cross}$)	a.u.
β_p	Total particle backscatter coefficient	km^{-1} sr^{-1}
β_i	Backscatter coefficient for a specific particle component (i)	km^{-1} sr^{-1}
$\overline{\beta_p}$	Height-integrated total particle backscatter coefficient	sr^{-1}

$\overline{\beta_i}$	Height integrated backscatter coefficient for a specific particle component (i)	sr^{-1}
β_{mol}	Molecular backscatter coefficient	km^{-1} sr^{-1}
Δ	Root square differences (see Eq. 8)	km^{-1} sr^{-1}
$\tilde{\Delta}$	Root mean square differences (see Eq. 10)	sr^{-1}
δ^V	Linear volume depolarization ratio	---
δ_p	Linear particle depolarization ratio	---
δ_i	Linear particle depolarization ratio for a specific particle component (i)	---
δ_{mol}	Molecular depolarization ratio	---
δ_{Df+ND}	Total fine (Df+ND) depolarization ratio (residual depolarization ratio)	---
δ^c_{Df+ND}	Columnar total fine (Df+ND) depolarization ratio	---
R	Backscattering ratio ($= \frac{\beta_{mol}+\beta_p}{\beta_{mol}}$)	---
S_a	Lidar Ratio (LR) (KF-derived)	sr
σ_p	Total particle extinction coefficient	km^{-1}
σ_i	Extinction coefficient for a specific particle component (i)	km^{-1}
AOD	Aerosol Optical Depth (total particle extinction, AERONET data)	---
AEx	Angstrom Exponent (AERONET data)	---
k_{eff}	Effective Mass Extinction Efficiency (MEE)	m^2 g^{-1}
k_i	Mass Extinction Efficiency for a specific particle component (i)	m^2 g^{-1}
c_{v_x}	Extinction-to-volume conversion factor for a specific particle size mode	10^{-12} Mm
VC_x	Volume concentration for a specific particle size mode (AERONET data)	10^{-12} Mm
τ_x	Extinction for a specific particle size mode (AERONET data)	---
TMC	Total Mass Concentration	g m^{-3}
M_i	Mass concentration for a specific particle component (i)	g m^{-3}
$\overline{TMC}$	Total mass loading (height-integrated TMC, over-bar is removed for simplicity)	g m^{-2}
$\overline{M_i}$	Mass loading (height-integrated M_i) for a specific particle component (i)	g m^{-2}

(*) i denotes the aerosol component: dust coarse (Dc), dust fine (Df), non-dust (ND), smoke (SM), non-smoke (NS), pollen (PL), background aerosols (BA).
(**) x denotes the particle size mode: coarse (c), fine (f).

Acknowledgements

This work is supported by the Spanish Ministerio de Economía y Competitividad (MINECO) under grant CGL2014-55230-R (AVATAR project) and the ACTRIS-2 (Aerosols, Clouds, and Trace Gases Research Infrastructure Network) Research Infrastructure Project funded by the European Union's Horizon 2020 research and innovation programme (grant agreement n. 654109). Lidar measurements in Barcelona were also supported by the Spanish MINECO (project TEC2015-63832-P) and EFRD (European Fund for Regional Development); by the Department of

Economy and Knowledge of the Catalan autonomous government (grant 2014 SGR 583); and the Unidad de
Excelencia Maria de Maeztu (project MDM-2016-0600) financed by the Spanish Agencia Estatal de Investigación.
The MPLNET project is funded by the NASA Radiation Sciences Program and Earth Observing System. The authors
gratefully acknowledge the NOAA Air Resources Laboratory (ARL) for the provision of the HYSPLIT transport and
dispersion model and/or READY website (http://www.ready.noaa.gov) used in this publication. C. C.-J. thanks the
Ministerio de Educación, Cultura y Deporte (MECD) support under grant PRX15/00375 for the 3-month research stay
at TROPOS (Germany); and A. del A. thanks the MINECO support (Programa de Ayudas a la Promoción del Empleo
Joven e Implantación de la Garantía Juvenil en i+D+i) under grant PEJ-2014-A-52129.

References

Ansmann, A., Tesche M., Seifert P., Groß, S., Freudenthaler, V., Apituley, A., Wilson, K. M., Serikov, I., Linné , H., Heinold, B., Hiebsch, A., Schnell, F., Schmidt, J., Mattis, I., Wandinger, U., and Wiegner, M.: Ash and fine mode particle mass profiles from EARLINET-AERONET observations over central Europe after the eruptions of the Eyjafjallajökull volcano in 2010, J. Geophys. Res., 116, D00U02, doi: 10.1029/2010JD015567, 2011.

Ansmann, A., Seifert, P., Tesche, M., and Wandinger, U.: Profiling of fine and coarse particle mass: case studies of Saharan dust and Eyjafjallajökull/Grimsvötn volcanic plumes, Atmos. Chem. Phys., 12, 9399–9415, doi:10.5194/acp-12-9399-2012, 2012.

Behrendt, A. and Nakamura, T.: Calculation of the calibration constant of polarization lidar and its dependency on atmospheric temperature, Optics Express, 10, 805–817, 2002.

Belmonte, J., Personal Communication, Institut de Ciència i Tecnologia Ambientals, Universitat Autònoma de Barcelona, Spain, 2016.

Böckmann, C., Mironova, I., Müller, D., Schneidenbach, L., Nessler, R: Microphysical aerosol parameters from multiwavelength lidar, J. Opt. Soc. Am. A, 22, 518–528, 2005.

Boucher, O., D. Randall, P. Artaxo, C. Bretherton, G. Feingold, P. Forster, V.-M. Kerminen, Y. Kondo, H. Liao, U. Lohmann, P. Rasch, S.K. Satheesh, S. Sherwood, B. Stevens and X.Y. Zhang: Clouds and Aerosols. In: Climate Change 2013: The Physical Science Basis. Contribution of Working Group I to the Fifth Assessment Report of the Intergovernmental Panel on Climate Change, Stocker, T.F., D. Qin, G.-K. Plattner, M. Tignor, S.K. Allen, J. Boschung, A. Nauels, Y. Xia, V. Bex and P.M. Midgley (Eds.), Cambridge University Press, Cambridge, United Kingdom and New York, NY, USA, 2013.

Burton, S. P., Ferrare, R. A., Hostetler, C. A., Hair, J. W., Rogers, R. R., Obland, M. D., Butler, C. F., Cook, A. L., Harper, D. B., and Froyd, K. D.: Aerosol classification using airborne High Spectral Resolution Lidar measurements – methodology and examples, Atmos. Meas. Tech., 5, 73-98, https://doi.org/10.5194/amt-5-73-2012, 2012.

Burton, S. P., M. A. Vaughan, R. A. Ferrare, and C. A. Hostetler: Separating mixtures of aerosol types in airborne High Spectral Resolution Lidar data, Atmos. Meas. Tech., 7, 419–436, 2014.

Cairo F, Di Donfrancesco G, Adriani A, Pulvirenti L, Fierli F.: Comparison of various depolarization parameters measured by lidar, Appl. Optics, 38, 4425–4432, 1999.

Campbell, J. R., Hlavka, D. L., Welton, E. J., Flynn, C. J., Turner, D. D., Spinhirne, J. D., Stanley Scott III, V., and Hwang, I. H.: Full-time, eye-safe cloud and aerosol Lidar observation at atmospheric radiation measurement program sites: Instruments and data processing, J. Atmos. Ocean. Tech., 19, 431–442, 2002.

Cecchi, L.: From pollen count to pollen potency: the molecular era of aerobiology, Eur. Respir. J., 42, 898–900, doi:10.1183/09031936.00096413, 2013.

Chaikovsky, A., Dubovik, O., Holben, B., Bril, A., Goloub, P., Tanré, D., Pappalardo, G., Wandinger, U., Chaikovskaya, L., Denisov, S., Grudo, J., Lopatin, A., Karol, Y., Lapyonok, T., Amiridis, V., Ansmann, A., Apituley, A., Allados-Arboledas, L., Binietoglou, I., Boselli, A., D'Amico, G., Freudenthaler, V., Giles, D., Granados-Muñoz, M. J., Kokkalis, P., Nicolae, D., Oshchepkov, S., Papayannis, A., Perrone, M. R., Pietruczuk, A., Rocadenbosch, F., Sicard, M., Slutsker, I., Talianu, C., De Tomasi, F., Tsekeri, A., Wagner, J., and Wang, X.: Lidar-Radiometer Inversion Code (LIRIC) for the retrieval of vertical aerosol properties from combined lidar/radiometer data: development and distribution in EARLINET, Atmos. Meas. Tech., 9, 1181–1205, doi: 10.5194/amt-9-1181-2016, 2016.

Chen, Y., Quan, H., Dong, X., Sugimoto, N., Matsui, I., and Shimizu, A.: Continuous measurement of dust aerosols with a dual-polarization lidar in Beijing, in Proceedings of Nagasaki Workshop on Aerosol-Cloud Radiation Interaction and Asian Lidar Network, pp. 28– 31, Cent. for Environ. Remote Sens., Chiba Univ., Chiba, Japan, 2001.

Córdoba-Jabonero, C., Adame, J.A., Grau, D., Cuevas, E., and Gil-Ojeda, M.: Lidar Ratio discrimination retrieval in a two-layer aerosol system from elastic lidar measurements in synergy with sun-photometry data. In: Proceedings of the International Conference in Atmospheric Dust, ProScience, 1, 243-248, 2014.

Córdoba-Jabonero, C., Andrey-Andrés, J., Gómez, L., Adame, J.A., Sorribas, M., Navarro-Comas, M., Puentedura, O., Cuevas, E., and Gil-Ojeda, M.: Vertical mass impact and features of Saharan dust intrusions derived from ground-based remote sensing in synergy with airborne in-situ measurements, Atmospheric Environment, 142, 420-429, 2016.

Dockery D., Pope C., Xu, X., Spengler, J., Ware, J., Fay, M., Ferris, B., and Speizer, F.: An association between air pollution and mortality in six US cities, New Engl. J. Med., 329, 1753–1759, 1993.

Dubovik, O., Lapyonok, T., Litvinov, P., Herman, M., Fuertes, D., Ducos, F., Lopatin, A., Chaikovsky, A., Torres, B., Derimian, Y., Huang, X., Aspetsberger, M., and Federspiel, C.: GRASP: a versatile algorithm for characterizing the atmosphere, SPIE: Newsroom, doi: 10.1117/2.1201408.005558, Published Online: September 19, 2014. http://spie.org/x109993.xml, 2014.

Fernald, F. G.: Analysis of atmospheric lidar observations: some comments, Appl. Optics, 23, 652–653, 1984.

Flynn, C., Mendoza, A., Zheng, Y., and Mathur, S.: Novel polarization-sensitive micropulse lidar measurement technique, Optics Express, 15 (6), 2785-2790, 2007.

Heintzenberg, J., Hermann, M., Weigelt, A., Clarke, A., Kapustin, V., Anderson, B., Thornhill, K., Van Velthoven, P., Zahn, A. and Brenninkmeijer, C.: Near-global aerosol mapping in the upper troposphere and lowermost stratosphere with data from the CARIBIC project. Tellus B, 63: 875–890. doi: 10.1111/j.1600-0889.2011.00578.x, 2011.

Hess, M., Koepke, P., Schult, I.: Optical properties of aerosols and clouds: the software package OPAC, Bull. Am. Meteorol. Soc., 79, 831-844, 1998.

725   Holben, B. N.,T F. Eck, I. Slutsker, D Tanre, JP Buis, A Setzer, E Vermote, JA Reagan, YJ Kaufman, T Nakajima, F. Lavenu, I Jankowiak, and A Smirnov: AERONET—A federated instrument network and data archive for aerosol characterization, Remote sensing of environment 66 (1), 1-16, 1999.

Ichoku, C., and Kaufman, Y. J.: A method to derive smoke emission rates from MODIS fire radiative energy measurements, IEEE Trans. Geosci. Remote, 43, 2636–2649, 2005.

730   Klett, J. D.: Lidar inversion with variable backscatter/extinction ratios, Appl. Optics, 24, 1638–1643, 1985.

Jackson, S.T., Lyford, M.E.: Pollen dispersal models in quaternary plant ecology: assumptions, parameters, and prescriptions, Bot. Rev. 65, 39-75, 1999.

Künzli, N., Kaiser, R., Medina, S., Studnicka, M., Chanel, O., Filliger, P., Herry, M., Horak, F. Jr., Puybonnieux-Texier, V., Quénel, P., Schneider, J., Seethaler, R., Vergnaud, J.-C., and Sommer, H.: Public health impact of outdoor
735   and traffic-related air pollution: a tri-national European assessment, Lancet, 356, 795–801, 2000.

Lopatin, A., Dubovik, O., Chaikovsky, A., Goloub, P., Lapyonok, T., Tanré, D., and Litvinov, P.: Enhancement of aerosol characterization using synergy of lidar and sun-photometer coincident observations: the GARRLiC algorithm, Atmos. Meas. Tech., 6, 2065–2088, doi: 10.5194/amt-6-2065-2013, 2013.

Mamouri,R. E., and Ansmann, A.: Fine and coarse dust separation with polarization lidar, Atmos. Meas. Tech., 7,
740   3717-3735, 2014.

Mamouri, R. E., and Ansmann, A.: Estimated desert-dust ice nuclei profiles from polarization lidar: methodology and case studies, Atmos. Chem. Phys., 15, 3463-3477, doi: 10.5194/acp-15-3463-2015, 2015.

Mamouri, R.-E., and Ansmann, A.: Potential of polarization lidar to provide profiles of CCN- and INP-relevant aerosol parameters, Atmos. 15 Chem. Phys., 16, 5905-5931, doi: 10.5194/acp-16-5905-2016, 2016.

745   Mamouri R. E., and Ansmann, A.: Potential of polarization/Raman lidar to separate fine dust, coarse dust, maritime, and anthropogenic aerosol profiles, Atmos. Meas. Tech., 10, 3403-3427, doi.org/10.5194/amt-10-3403-2017, 2017.

Martiny, N., and Chiapello, I.: Assessments for the impact of mineral dust on the meningitis incidence in West Africa. Atmos Environ 70:245–253; doi: 10.1016/j.atmosenv.2013.01.016, 2013.

Müller, D., Wandinger, U., and Ansmann, A.: Microphysical particle parameters from extinction and backscatter lidar
750   data by inversion with regularization: Theory, Appl. Opt., 38, 2346–2357, 1999.

Müller, D., Mattis, I., Wandinger, U., Ansmann, A., and Althausen, D.: Raman lidar observations of aged Siberian and Canadian forest fire smoke in the free troposphere over Germany in 2003: Microphysical particle characterization, J. Geophys. Res., 110, D17201, doi: 10.1029/2004JD005756, 2005.

Myhre, G., D. Shindell, F.-M. Bréon, W. Collins, J. Fuglestvedt, J. Huang, D. Koch, J.-F. Lamarque, D. Lee, B.
755   Mendoza, T. Nakajima, A. Robock, G. Stephens, T. Takemura and H. Zhang: Anthropogenic and Natural Radiative Forcing. In: Climate Change 2013: The Physical Science Basis. Contribution of Working Group I to the Fifth Assessment Report of the Intergovernmental Panel on Climate Change, Stocker, T.F., D. Qin, G.-K. Plattner, M. Tignor, S.K. Allen, J. Boschung, A. Nauels, Y. Xia, V. Bex and P.M. Midgley (Eds.), Cambridge University Press, Cambridge, United Kingdom and New York, NY, USA, 2013.

760 Noh, Y. M., Lee, H., Mueller, D., Lee, K., Shin, D., Shin, S., Choi, T. J., Choi, Y. J., and Kim, K. R.: Investigation of the diurnal pattern of the vertical distribution of pollen in the lower troposphere using LIDAR, Atmos. Chem. Phys., 13, 7619–7629, doi:10.5194/acp-13-7619-2013, 2013.

Pappalardo, G., Mona, L., D'Amico, G.,Wandinger, U., Adam, M., Amodeo, A., Ansmann, A., Apituley, A., Alados Arboledas, L., Balis, D., Boselli, A., Bravo-Aranda, J. A., Chaikovsky, A., Comeron, A., Cuesta, J., De Tomasi, F.,
765 Freudenthaler, V., Gausa, M., Giannakaki, E., Giehl, H., Giunta, A., Grigorov, I., Groß, S., Haeffelin, M., Hiebsch, A., Iarlori, M., Lange, D., Linné, H., Madonna, F., Mattis, I., Mamouri, R.-E., McAuliffe, M. A. P., Mitev, V., Molero, F., Navas-Guzman, F., Nicolae, D., Papayannis, A., Perrone, M. R., Pietras, C., Pietruczuk, A., Pisani, G., Preißler, J., Pujadas, M., Rizi, V., Ruth, A. A., Schmidt, J., Schnell, F., Seifert, P., Serikov, I., Sicard, M., Simeonov, V., Spinelli, N., Stebel, K., Tesche, M., Trickl, T., Wang, X., Wagner, F.,Wiegner, M., and Wilson, K. M.: Four-
770 dimensional distribution of the 2010 Eyjafjallajökull volcanic cloud over Europe observed by EARLINET, Atmos. Chem. Phys., 13, 4429–4450, doi:10.5194/acp-13-4429-2013, 2013.

Pérez, C., Nickovic, S., Baldasano, J. M., Sicard, M., Rocadenbosch, F., and Cachorro, V. E.: A long Saharan dust event over the western Mediterranean: Lidar, sun photometer observations, and regional dust modeling, J. Geophys. Res., 111, D15214, doi: 10.1029/2005JD006579, 2006.

775 Reid, J. S., Eck, T. F., Christopher, S. A., Koppmann, R., Dubovik, O., Eleuterio, D. P., Holben, B. N., Reid, E. A., and Zhang, J.: A review of biomass burning emissions part III: intensive optical properties of biomass burning particles, Atmos. Chem. Phys., 5, 827–849, 2005.

Rocadenbosch, F., Dhiraj, K., Lange, D., Gregorio, E., Frasier, S., and Sicard, M.: Backscatter error bounds for the elastic lidar two-component inversion algorithm, IEEE Trans. Geosci. Remote Sens., 50 (11), 4791-4803, doi:
780 10.1109/TGRS.2012.2194501, 2012.

Rodríguez-Gómez, A., Sicard, M., Granados-Muñoz, M.J., Ben Chahed, E., Muñoz-Porcar, C., Barragan, R., Comerón, A., Rocadenbosch, F., and Vidal, E.: An Architecture Providing Depolarization Ratio Capability for a Multi-Wavelength Raman Lidar: Implementation and First Measurements, Sensors, 17, 2957, doi: 10.3390/s17122957, 2017.

785 Sassen, K.: The Polarization Lidar Technique for Cloud Research: A Review and Current Assessment, Bull. Amer. Meteor. Soc., 72, 1848–1866, https://doi.org/10.1175/1520-0477(1991)072<1848:TPLTFC>2.0.CO;2, 1991.

Shimizu, A., Sugimoto, N., Matsui, I., Arao, K., Uno, I., Murayama, T., Kagawa, N., Aoki, K., Uchiyama, A., and Yamazaki, A.: Continuous observations of Asian dust and other aerosols by polarization lidars in China and Japan during ACE-Asia, J. Geophys. Res., 109, D19S17, doi: 10.1029/2002JD003253, 2004.

790 Sigma Space Corporation, Micro Pulse Lidar System Instruction Manual, MPL-4B-IDS Series, 4600 Forbes Blvd., Lanham, MD 20706, USA, August 2012.

Sicard, M., Rocadenbosch, F., Reba, M. N. M., Comerón, A., Tomás, S., García-Vízcaino, D., Batet, O., Barrios, R., Kumar, D., and Baldasano, J. M.: Seasonal variability of aerosol optical properties observed by means of a Raman lidar at an EARLINET site over Northeastern Spain, Atmos. Chem. Phys., 11, 175–190, doi:10.5194/acp-11-175-
795 2011, 2011.

Sicard, M., Guerrero-Rascado, J. L., Navas-Guzmán, F., Preißler, J., Molero, F., Tomás, S., Bravo-Aranda, J. A., Comerón, A., Rocadenbosch, F.,Wagner, F., Pujadas, M., and Alados-Arboledas, L.: Monitoring of the Eyjafjallajökull volcanic aerosol plume over the Iberian Peninsula by means of four EARLINET lidar stations, Atmos. Chem. Phys., 12, 3115–3130, doi: 10.5194/acp-12-3115-2012, 2012.

800 Sicard, M., D'Amico, G., Comerón, A., Mona, L., Alados-Arboledas, L., Amodeo, A., Baars, H., Baldasano, J. M., Belegante, L., Binietoglou, I., Bravo-Aranda, J. A., Fernández, A. J., Fréville, P., García-Vizcaíno, D., Giunta, A., Granados-Muñoz, M. J., Guerrero-Rascado, J. L., Hadjimitsis, D., Haefele, A., Hervo, M., Iarlori, M., Kokkalis, P., Lange, D., Mamouri, R. E., Mattis, I., Molero, F., Montoux, N., Muñoz, A., Muñoz Porcar, C., Navas-Guzmán, F., Nicolae, D., Nisantzi, A., Papagiannopoulos, N., Papayannis, A., Pereira, S., Preißler, J., Pujadas, M., Rizi, V.,

805 Rocadenbosch, F., Sellegri, K., Simeonov, V., Tsaknakis, G., Wagner, F., and Pappalardo, G.: EARLINET: potential operationality of a research network, Atmos. Meas. Tech., 8, 4587–4613, doi: 10.5194/amt-8-4587-2015, 2015.

Sicard, M., Izquierdo, R., Alarcón, M., Belmonte, J., Comerón, A., and Baldasano, J. M.: Near-surface and columnar measurements with a micro pulse lidar of atmospheric pollen in Barcelona, Spain, Atmos. Chem. Phys., 16, 6805-6821, doi: 10.5194/acp-16-6805-2016, 2016a.

810 Sicard, M., Izquierdo, R., Jorba, O., Alarcón, M., Belmonte, J., Comerón, A., Baldasano, J. M.; Atmospheric dispersion of airborne pollen evidenced by near-surface and columnar measurements in Barcelona, Spain, Proc. SPIE 10001, 100010L, A. Comerón, E. I. Kassianov, K. Schäfer, J. W. Jack, R. H. Picard, K. Weber (Ed.), SPIE, Washington (EE.UU.), doi: 10.1117/12.2244517, Edinburgh, United Kingdom, 26 – 29 September 2016, 2016b.

Stein, A.F., Draxler, R.R, Rolph, G.D., Stunder, B.J.B., Cohen, M.D., and Ngan, F.: NOAA's HYSPLIT atmospheric

815 transport and dispersion modeling system, Bull. Amer. Meteor. Soc., 96, 2059-2077, http://dx.doi.org/10.1175/BAMS-D-14-00110.1, 2015.

Tesche, M., Groß, S., Ansmann, A., Müller, D., Althausen, D.,Freudenthaler, V., and Esselborn, M.: Profiling of Saharan dust and biomass-burning smoke with multiwavelength polarization Raman lidar at Cape Verde, Tellus B, 63, 649–676,doi:10.1111/j.1600-0889.2011.00548.x, 2011.

820 Veselovskii, I., Kolgotin, A., Griaznov, V., Müller, D.,Wandinger, U., Whitemann, D.N.: Inversion with regularization for the retrieval of tropospheric aerosol parameters from multiwavelength lidar sounding, Appl. Opt., 41, 3685–3699, 2002.

Welton, E. J., and Campbell J. R.: Micropulse Lidar Signals: Uncertainty Analysis, J. Atmos. Oceanic Technol., 19, 2089-2094, 2002.

825 WHO: Health aspects of air pollution with particulate matter, ozone and nitrogen dioxide, World Health Organization, Report EUR/03/5042688, 1-98, 2003.

Zhang, R., Duhl, T., Salam, M.T., House, J.M., Flagan, R. C., Avol, E.L., Gilliland, F.D., Guenther, A., Chung, S. H., Lamb, B.K., and Van Reken, T.M.: Development of a regional-scale pollen emission and transport modeling framework for investigating the impact of climate change on allergic airway disease, Biogeosciences 11, 1461–1478,

830 doi:10.5194/bg-11-1461-2014, 2014.

835 **Table 1. Relative uncertainties for the P-MPL-derived particle optical properties (at 532 nm wavelength), and mass concentrations. (n) and (d) stand for night-time and day-time P-MPL measurements, respectively.**

Parameter	Symbol (*)	Relative uncertainty (%)	References
Particle backscatter coefficient (km^{-1} sr^{-1})	β_p	5 - 20 (n), 10 - 30 (d)	Rocadenbosch et al. (2012)
Particle extinction coefficient (km^{-1})	σ_p	10 – 30 (n), 15 – 40 (d)	Derived from the errors in β_p and LR
Lidar ratio (sr)	LR	5 - 10	Derived from KF algorithm
Particle linear depolarization ratio	δ_p	10 - 60	Rodríguez-Gómez et al. (2017)
Volume linear depolarization ratio	δ^V	10 - 50	Derived from the errors in both $pRCS$ and $sRCS$
Total Mass Concentration (g m^{-3})	TMC	10 - 40	Derived from the error in AOD ($=\sum_z \sigma_p(z)$), mainly

(*) As denoted in the text.

840

Table 2. Aerosol cases observed over BCN on selected days. AERONET data at particular times of the event (as shown in Figs. 4, 6 and 8), including those KF-retrieved LR values (S_a), and parameters used in the POLIPHON retrieval algorithm, depending on the version applied. References for the assumed particle linear depolarization ratio for specific components are also included δ_i (either i = 1-3, or i = 1, 2, depending on the case) are also included. Errors are shown in parenthesis.

Aerosol case Date	Time (UTC)	S_a (sr)	AERONET data		POLIPHON retrieval (*)	Linear depolarization ratio for each aerosol component (**)			
			AOD	AEx		δ_1	δ_2	δ_3	Reference
DUST 05 July 2016	02:00	50	0.33	0.52	POL-1	0.31	0.05	---	Tesche et al. (2011); Ansmann et al. (2012)
		(10)	(0.01)	(0.03)		(DD)	(ND)		
	16:00	29	0.25	1.70	POL-2	0.39	0.16	0.05	Mamouri and Ansmann (2014)
		(6)	(0.01)	(0.01)		(Dc)	(Df)	(ND)	
SMOKE 23 May 2016	06:00	81	0.14	1.30	POL-1	0.15	0.05	---	Groβ et al. (2013)
		(16)	(0.02)	(0.24)		(SM)	(BA)		
	14:00	45	0.16	0.72					
		(9)	(0.01)	(0.05)					
POLLEN 23 March 2016	10:00	98	0.12	0.75	POL-1	0.40	0.05	---	Sicard et al. (2016)
		(20)	(0.01)	(0.02)		(PL)	(BA)		
	15:00	39	0.10	1.74					
		(8)	(0.01)	(0.03)					

(*) POL-1: Separation of two components; POL-2: Separation of three components.

(**) Particular δ_i values assumed for each specific aerosol component (i), regarded as 'pure' aerosols: Dc, Df and ND stand, respectively, for dust coarse, dust fine and non-dust particles; SM and NS stand, respectively, for smoke and non-smoke aerosols; and PL and BA stand, respectively, for pollen particles and local background aerosols.

Table 3. Parameters involved in the extinction-to-mass conversion for each aerosol case: the AERONET-reported and derived mass conversion factors (c_v), the assumed particle densities (Pd), and the Mass Extinction Efficiency (k) values. For the dust case (3-component separation): i = 1 (Dc), 2 (Df) and 3 (ND); and for the smoke / pollen cases (2-component separation), respectively: i = 1 (SM / PL) and 2 (NS / BA). Errors are shown in parenthesis.

Aerosol case	Time (UTC)	AERONET data (*) VC_c VC_f	τ_c τ_f	c_v (10^{-12} Mm) 1	2	3	Pd (g cm^{-3})	k (m^2 g^{-1}) 1	2	3	eff
DUST (POL-1/2)	02:00	0.192 (0.003) 0.022 (0.009)	0.237 (0.006) 0.100 (0.003)	0.81 (0.03)	0.20 (0.09)	--- (---)	2.60 (Dc, Df) 1.80 (ND)	0.47 (0.02)	2.0 (0.9)	--- (---)	0.57 (0.07)
	16:00	0.062 (0.003) 0.040 (0.003)	0.092 (0.003) 0.181 (0.001)	0.67 (0.05)	0.25 (0.02)	0.20 (0.01)		0.57 (0.05)	1.5 (0.1)	2.7 (0.1)	1.6 (0.2)
SMOKE (POL-1)	06:00	0.005 (0.001) 0.021 (0.006)	0.024 (0.001) 0.122 (0.002)	0.17 (0.05)	0.21 (0.05)	---	1.30 (SM) 2.00 (NS)	4.5 (1.4)	2.4 (0.5)	---	3.5 (1.5)
	14:00	0.049 (0.001) 0.027 (0.006)	0.062 (0.001) 0.066 (0.001)	0.41 (0.10)	0.79 (0.03)	---		1.9 (0.5)	0.63 (0.02)	---	2.1 (0.4)
POLLEN (POL-1)	10:00	0.013 (0.002) 0.012 (0.002)	0.058 (0.010) 0.054 (0.001)	0.22 (0.07)	0.22 (0.04)	---	0.92 (PL) (*Platanus*) 1.80 (BA)	4.9 (1.6)	2.5 (0.5)	---	4.1 (1.2)
	15:00	0.017 (0.001) 0.012 (0.001)	0.035 (0.001) 0.070 (0.004)	0.47 (0.03)	0.17 (0.02)	---		2.3 (0.1)	3.2 (0.5)	---	3.5 (1.0)

(*) 'c' and 'f' denote the particle coarse and fine modes, respectively.

Table 4. Height-integrated mass concentration ($\overline{M}_\iota$, i.e., mass loading, g m^{-2}) for each component and the total mass concentration (TMC) at two times for each aerosol case. Errors are shown in parenthesis.

Aerosol case	Time (UTC)	$\overline{M}$ (g m^{-2})			TMC (g m^{-2})
		1	2	3	
DUST	02:00	0.54 (0.04)	0.03 (0.02)	--- (---)	0.57 (0.05)
	16:00	0.08 (0.01)	0.026 (0.003)	0.057 (0.003)	0.16 (0.02)
SMOKE	06:00	0.012 (0.004)	0.027 (0.007)	---	0.04 (0.01)
	14:00	0.023 (0.006)	0.053 (0.004)	---	0.08 (0.01)
POLLEN	10:00	0.0009 (0.0003)	0.029 (0.006)	---	0.029 (0.006)
	15:00	0.011 (0.001)	0.017 (0.004)	---	0.028 (0.005)

870

875
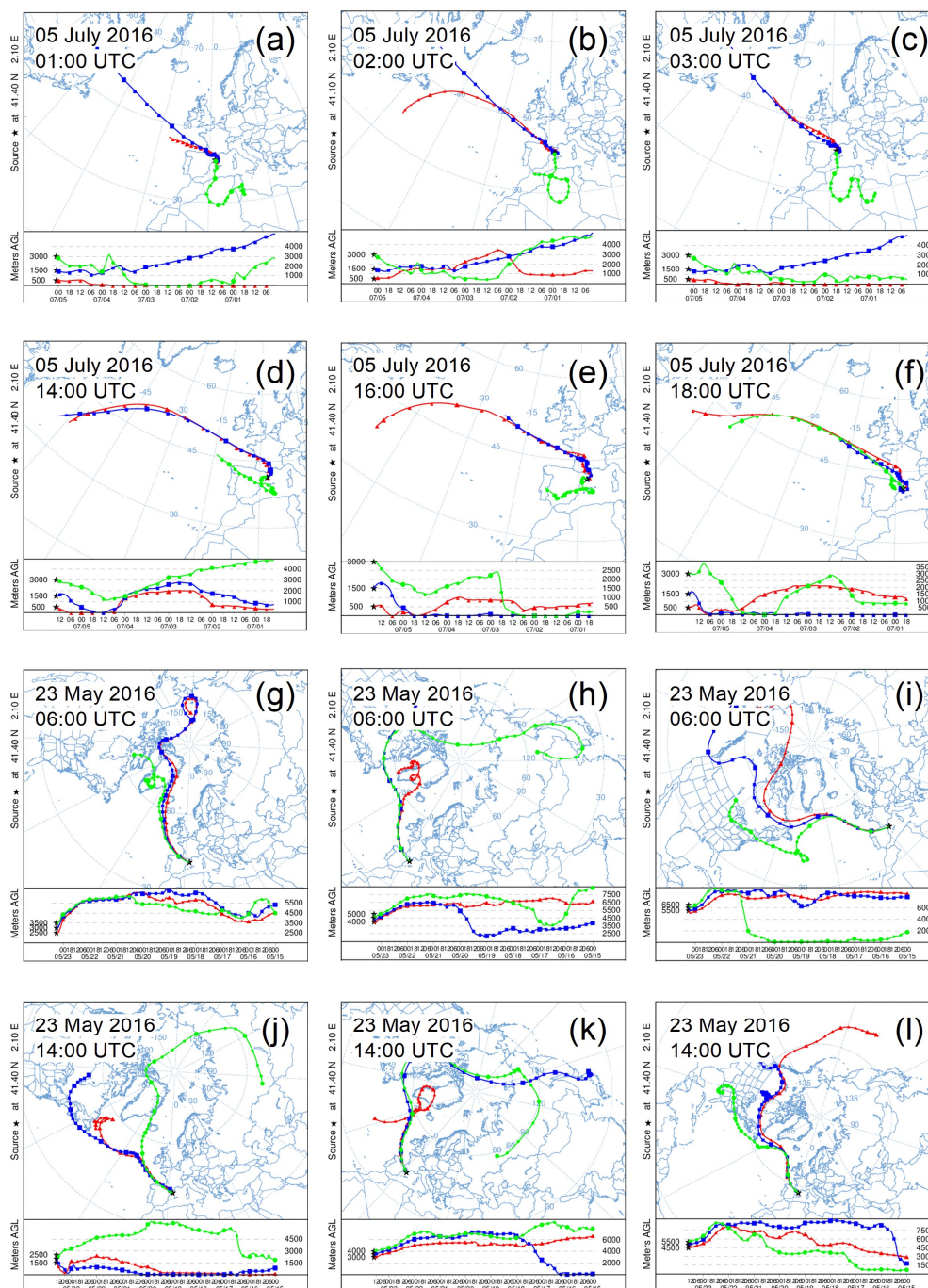
Figure 1: HYSPLIT backtrajectories ending at different altitudes over BCN depending on the aerosol case (only for the dust and smoke cases): (a) – (f) for dust (5 days back) on 5 July 2016; (g) - (l) for smoke (10 days back) on 23 May 2016. Selected times of the air masses arrivals are related to those aerosol profiles particularly examined (as shown in Sect. 3; in particular, see Figs. 4 and 6).

880
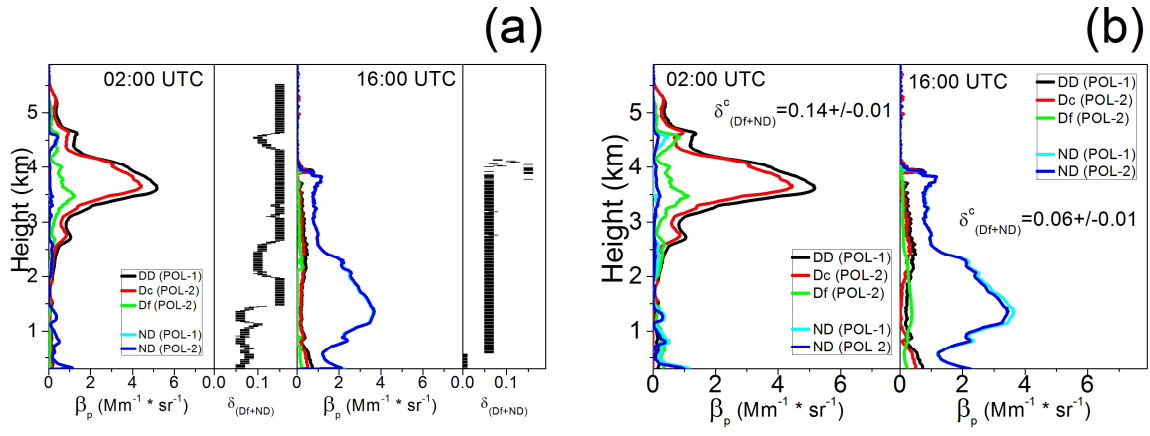
Figure 2. POL-1 versus POL-2 differences in particle backscatter coefficient profiles for each component (total dust β_{DD}, and non-dusty β_{ND} from POL-1; dust coarse β_{Dc} and fine β_{Df}, being $\beta_{Dc} + \beta_{Df} = \beta_{DD}$, and non-dusty β_{ND} from POL-2) retrieved for the dust case on 5 July 2016 at 02:00 and 16:00 UTC, respectively, by using (optimally-derived): (a) a $\delta_{Df+ND}(z)$.profile, and (b) a single columnar δ^c_{Df+ND} value.
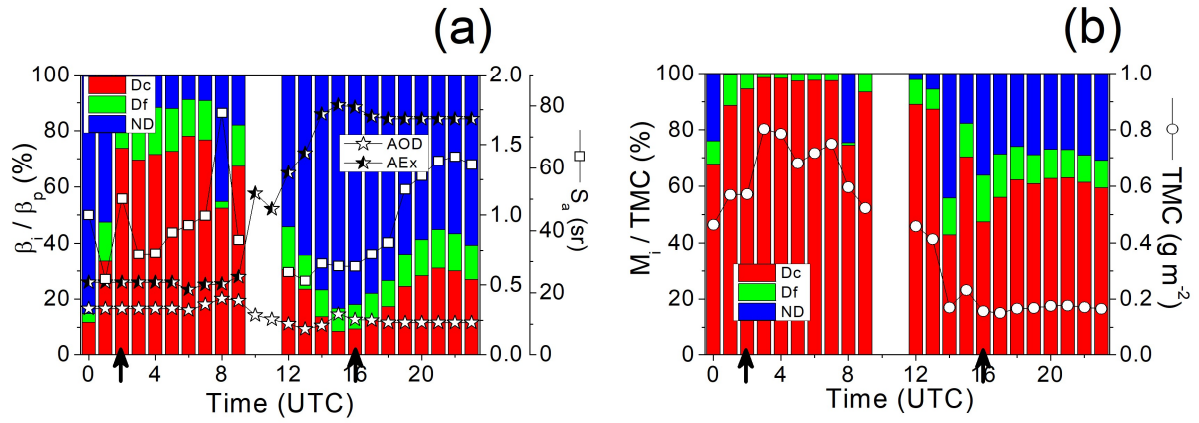
Figure 3. Dust event occurred on 5 July 2016. Evolution of the relative contribution (a) $\frac{\overline{\beta_i}}{\overline{\beta_p}}$ (%) and (b) $\overline{M_i}/TMC$ (%) (the bar over the variable are removed in the figure for clarity) for each aerosol component along the day: Dc (red bars), Df (green bars) and ND (blue bars) which denote, respectively, dust coarse, dust fine and non-dusty aerosols. In plot (a) (right axis) AERONET hourly-averaged AOD and AEx (white and black/white stars, respectively) and KF-derived S_a (lidar ratio, sr; square symbols) values are reported; in plot (b) (right axis) TMC (total mass loading, g m^{-2}; open circles) is also included. Black arrows on the time axis indicate selected times for those vertical profiles shown in Fig. 4.

905
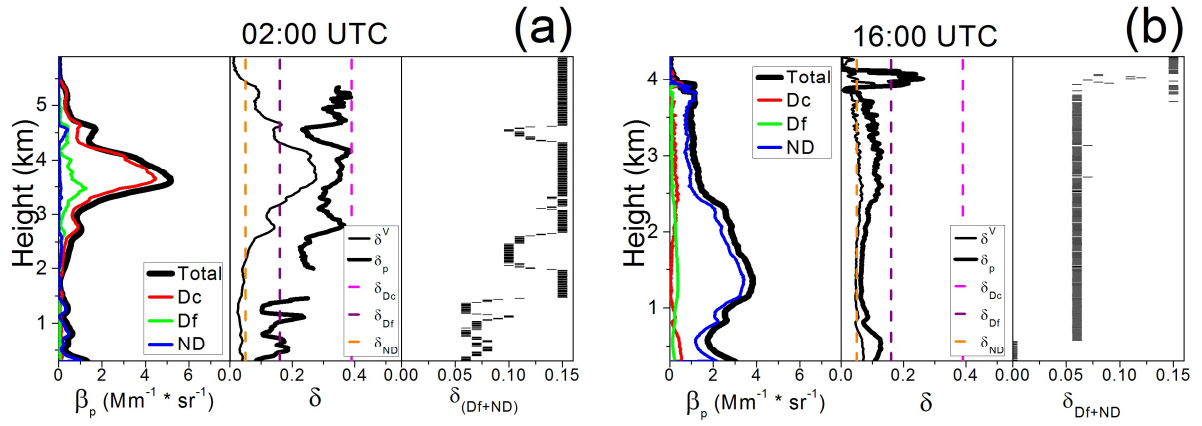
Figure 4. Dust event occurred on 5 July 2016. Vertical profiles of the particle backscatter coefficients (total and for each specific component; left panels), the linear depolarization ratios (volume δ^V and particle δ_p; centre panels), and the estimated depolarization ratio for the fine (Df+ND) mode (δ_{Df+ND}, right panels) at two times illustrating the different aerosol scenario observed along the day: (a) at 02:00 UTC (high dust incidence), and (b) at 16:00 UTC (low dust incidence).
910 **Specific depolarization ratios selected for each pure aerosol component are also shown by vertical dashed lines (see legend) in the centre panels.**

915
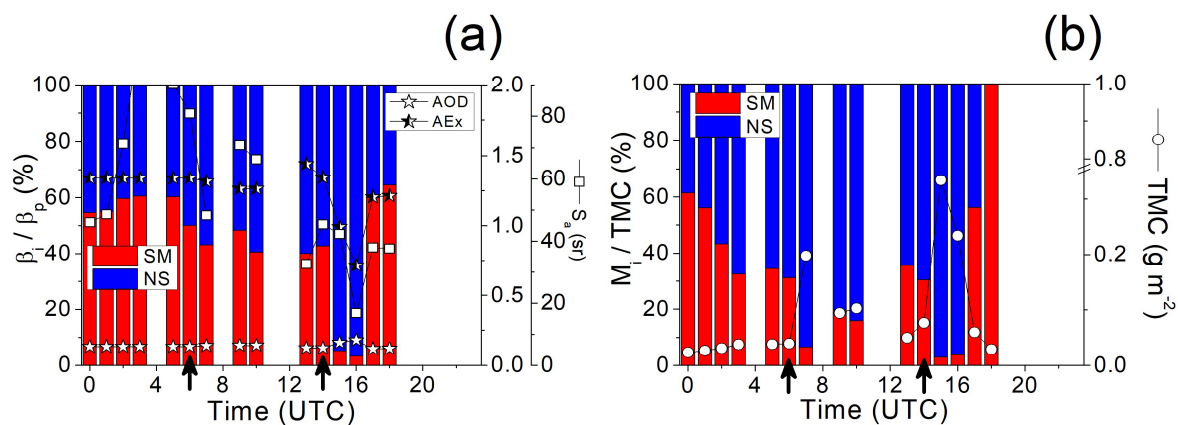
Figure 5. The same as Fig. 3, but for the smoke case occurred on 23 May 2016: SM (red bars) and NS (blue bars), which denote, respectively, smoke and non-smoke components. Black arrows on the time axis indicate selected times for those
920 **vertical profiles shown in Fig. 6.**

925
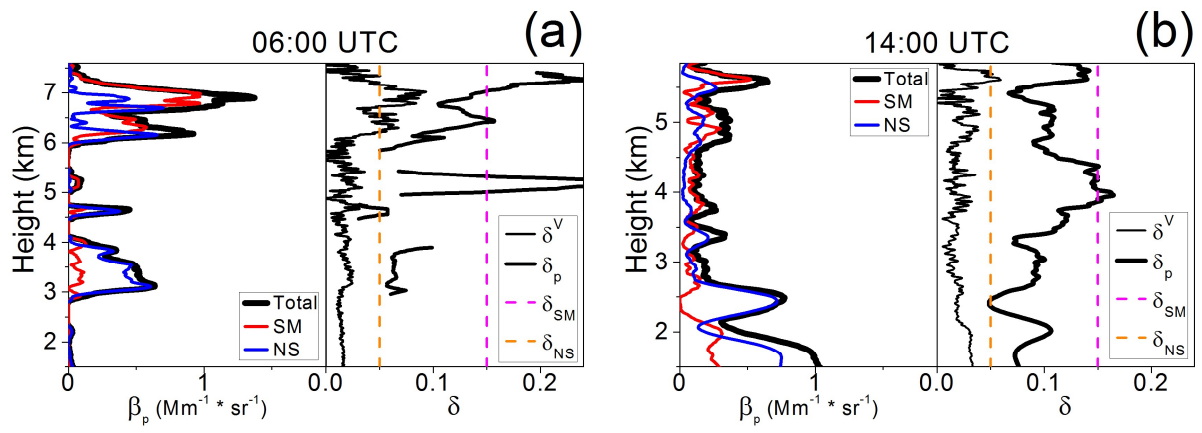
Figure 6. The same as Fig. 4, but for the smoke event occurred on 23 May 2016 at: (a) 06:00 UTC, and (b) 14:00 UTC.
930 **Specific depolarization ratios selected for each smoke aerosol component are also shown by vertical dashed lines (see legend for details).**

935
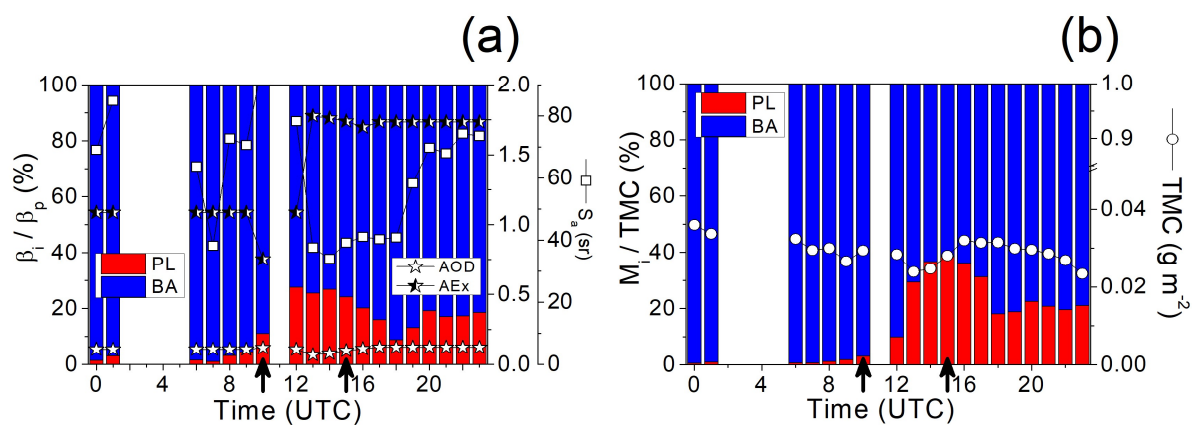
Figure 7. The same as Fig. 3, but for the pollen event occurred on 23 March 2016: PL (red bars) and BA (blue bars), which
940 **denote, respectively, pollen and local background aerosol components. Black arrows on the time axis indicate selected times for those vertical profiles shown in Fig. 8.**

945
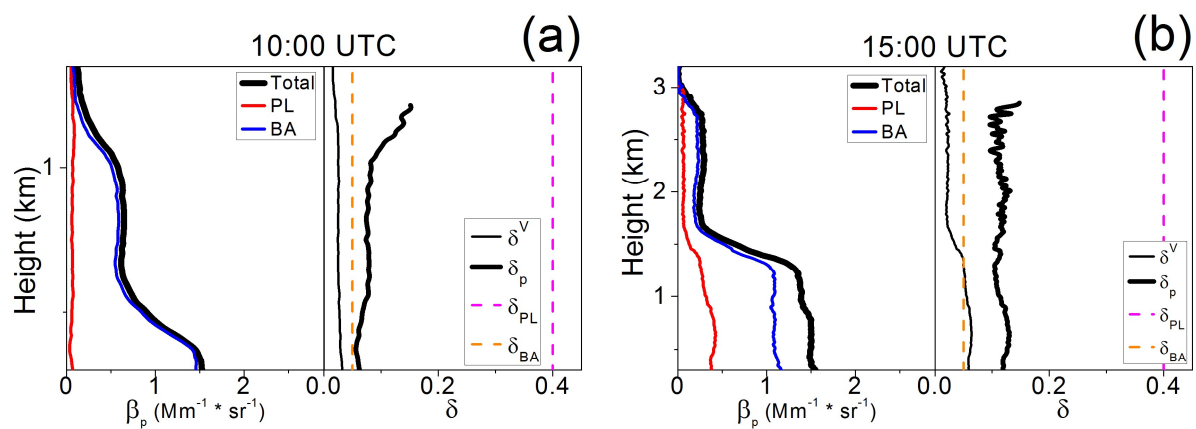
Figure 8. The same as Fig. 4, but for the pollen event occurred on 23 March 2016 at: (a) 10:00 UTC (no PL detection), and (b) 15:00 UTC (enhanced PL occurrence). Specific depolarization ratios selected for each pure aerosol component are also shown by vertical dashed lines (see legend for details).

950